Available online at www.sciencedirect.com

SciVerse ScienceDirect

Nuclear Physics A 879 (2012) 107–131

NUCLEAR PHYSICS A

www.elsevier.com/locate/nuclphysa

Observation of entrance channel mass-asymmetry effect on incomplete fusion reaction for ^{20}Ne + ^{165}Ho system

D. Singh [a,b], Rahbar Ali [b], M. Afzal Ansari [b,*], B.S. Tomar [c], M.H. Rashid [d], R. Guin [e], S.K. Das [e]

[a] *Nuclear Physics Group, Inter-University Accelerator Centre, New Delhi-110 067, India*
[b] *Nuclear Physics Laboratory, Department of Physics, Aligarh Muslim University, Aligarh-202 002, India*
[c] *Radio-chemistry Division, Bhabha Atomic Research Centre, Trombay, Mumbai-400085, India*
[d] *Accelerator Physics Group, Variable Energy Cyclotron Centre, 1/AF, Bidhan Nagar, Kolkata-700 064, India*
[e] *Radio-chemistry Group, Variable Energy Cyclotron Centre, 1/AF, Bidhan Nagar, Kolkata-700 064, India*

Received 12 May 2011; received in revised form 24 December 2011; accepted 26 January 2012

Available online 7 February 2012

Abstract

An experiment has been performed to explore the incomplete fusion (ICF) reaction dynamics in heavy ion induced reactions. Excitation functions (EFs) for eighteen evaporation residues (ERs) produced in the system ^{20}Ne + ^{165}Ho have been measured in the energy range $\approx$ 88–164 MeV. Some of the ERs have significant contribution from precursor decay, which has been separated out from the measured cumulative cross-sections to get direct production cross-sections. Parameters of the statistical model code PACE-2 are optimized to reproduce the ERs populated in complete fusion reactions such as in xn and pxn channels. Using the same parameters, EFs for the residues produced in α-particle(s) emission channels have been calculated. A significant enhancement in the measured EFs of the ERs produced in α-particle(s) emission channels over the PACE-2 predictions have been observed which indicates the occurrence of incomplete fusion reaction process. In the ICF process the break-up of projectile ^{20}Ne into ^{4}He + ^{16}O and/or ^{8}Be + ^{12}C takes place followed by fusion of one of the fragments with the target nucleus ^{165}Ho. The present data analyses suggest that probability of incomplete fusion reaction increases with projectile energy. The ICF fraction F^{ICF} has been estimated and found to increase with increasing mass-asymmetry $[A_T/(A_T + A_P)]$ of the partners in entrance channel. It is also observed that critical angular momentum associated with incomplete fusion channels at higher projectile energy may be associated with ℓ-values lower than that of peripheral collisions, indicating that the incomplete fusion competes with complete fusion even at angular momentum values little lower than critical angular momentum.

* Corresponding author.
E-mail addresses: dsinghiuac@gmail.com (D. Singh), drmafzalansari@yahoo.com (M. Afzal Ansari).

0375-9474/$ – see front matter
doi:10.1016/j.nuclphysa.2012.01.020

Keywords: NUCLEAR REACTIONS ^{165}Ho(^{20}Ne, 3n), (^{20}Ne, 2np), (^{20}Ne, 3np), (^{20}Ne, α), (^{20}Ne, 2nα), (^{20}Ne, 3nα), (^{20}Ne, 4nα), (^{20}Ne, 3npα), (^{20}Ne, 4npα), (^{20}Ne, 6npα), (^{20}Ne, n2pα), (^{20}Ne, 2α), (^{20}Ne, n2α), (^{20}Ne, 2n2α), (^{20}Ne, 3n2α), (^{20}Ne, 4n2α), (^{20}Ne, 3np2α), (^{20}Ne, 3n4α), $E = 88$–165 MeV; measured ER E_γ, I_γ using recoil catcher technique; deduced direct, cumulative yields, ICF σ, total σ, critical angular momentum, mass-asymmetry effect; calculated σ, yields; statistical model with Monte Carlo de-excitation with different level density parameters; ICF fraction compared with literature data for other systems

1. Introduction

The study of incomplete fusion (ICF) in heavy ion (HI) reactions particularly with heavier target nuclei above Coulomb barrier has been the subject of resurgent interest in nuclear physics in the recent years. The ICF cross-section as a function of entrance channel mass-asymmetry has been explained in terms of the model based on the interaction barrier, critical angular momentum and critical distance of approach [1]. At projectile energies slightly above the Coulomb barrier, both the complete fusion (CF) and incomplete fusion (ICF) are the dominant reaction mechanisms. In case of CF reaction the projectile completely fuses with the target nucleus and the highly excited nuclear system decays by evaporating low energy nucleons and alpha particles, and are explained by statistical model. In the ICF reaction process, which is characterized by the partial fusion of the projectile with the target, the projectile is assumed to break-up into two fragments (e.g. ^{20}Ne-ion may break-up into ^{16}O + ^{4}He and/or ^{12}C + ^{8}Be) and one of the fragments fuses with the target nucleus while remnant moves in the forward direction [2–4]. The excited composite system formed as a result of the fusion of the fragment of the incident ion with the target may also under go de-excitation by emission of particles and/or γ-rays. In recent years there has been growing experimental interest in the ICF reactions for studying neutron rich nuclei, which cannot be reached by CF process [5]. ICF phenomenon has been observed in low-Z projectile ($Z \leqslant 10$) e.g. ^{12}C, ^{14}N, ^{16}O and ^{20}Ne, in their interaction with medium and heavy mass targets [6–12]. The first experimental evidence of ICF reactions was given by Britt and Quinton [13], who observed the break-up of the incident projectiles like ^{12}C, ^{14}N and ^{16}O into alpha clusters in an interaction with the target nucleus at ≈ 10.5 MeV/A bombarding energy. Subsequently, Galin et al. [14] also observed the break-up of projectile and called such reactions, leading to the emission of "fast" alpha particles, as 'ICF reaction' or 'break-up fusion reaction'. However, major advances in the study of ICF reactions took place after the work of Inamura et al. [15] for ^{14}N + ^{159}Tb system at beam energy about ≈ 7 MeV/nucleon, wherein exclusive measurements of forward-peaked alpha-particles in coincidence with the prompt gamma-rays of the different ERs produced, were done. Parker et al. [16] observed ICF in the reactions at 5 MeV/A ^{12}C-beam on ^{51}V by measuring the forward peaked α-particles in the energy spectra and angular distribution of α-particles. Tserruya et al. [17] also found evidence for ICF process from time-of-flight measurements of ERs in a reaction of 5–10 MeV/A ^{12}C-beam with ^{120}Sn, ^{160}Gd and ^{197}Au. The ICF studies using loosely bound projectiles have also been done by Gomes et al. [18]. It has also been observed that ICF of the projectile occurs at beam energies below 10 MeV/nucleon. As a matter of fact, a large number of out going reaction channels are opened in heavy ion induced reactions at moderate excitation energies and the analysis of EFs of the ERs may provide significant information about the CF and ICF reactions. Vergani et al. [19], Cavinato et al. [20], Crippa et al. [21], Tomar et al. [22], Gupta et al. [23], Sharma et al. [10], Ali et al. [24] and Singh et al. [25] have also measured the EFs and forward recoil range distributions (RRDs) of the ERs produced in CF and ICF of heavy-ions using recoil catcher activation

technique for a large number of projectile-target systems. From the analysis of measured EFs, it has been shown that ICF process has a substantial contribution to the reaction cross-sections. Earlier Morgestern et al. [26] carried out experiments on a various projectile target combinations have brought out the entrance channel mass-asymmetry dependence of ICF reaction, with ICF probability being higher in a mass-asymmetric system than mass-symmetric system at the same relative velocity. Later on, studies by Vineyard et al. [27], Chakrabarty et al. [28] and Ali et al. [24] also supported the findings of Morgestern et al. [26]. However, their studies are limited to few projectile-target combinations and systematic measurements are still demanded. Some of the characteristic features of ICF dynamics are: (i) ICF reactions are observed generally in low-Z projectiles ($Z \leqslant 10$), (ii) production cross-sections for ICF products are found to be larger than predicted by fusion-evaporation (CF) models, (iii) ICF residues traverse smaller distances in the stopping medium than that of CF residues, (iv) projectile like fragments (PLFs) produced in the ICF are mostly concentrated in the forward cone, (v) spin distributions for ICF residues are found to be distinctly different in nature from those of CF residues and the input angular momentum associated with ICF is found to be little larger than those associated with CF reaction.

Several models have been proposed to explain ICF reaction dynamics. The break-up fusion (BUF) model of Udagawa and Tamura [29] based on DWBA formalism explained ICF in terms of break-up of the projectile in the nuclear field (e.g. projectile ^{20}Ne may break-up into $^{16}\mathrm{O} + {}^{4}\mathrm{He}$ and/or $^{12}\mathrm{C} + {}^{8}\mathrm{Be}$) as it approaches to the nuclear field of target nucleus. It is assumed that one of the fragments may fuse with the target nucleus, while the remnant moves as a spectator and gives rise to projectile like fragments (PLFs). The Sumrule model of Wilczynski et al. [30] assumes that the various ICF channels are localized in the angular momentum space above the critical angular momentum for the CF of the projectile and target. Other models include promptly emitted particle (PEP) model [31], hot spot model [32], and multistep direct reaction model [33]. In fact, all the existing models have been used to fit the experimental data above 10 MeV/nucleon energies. However, at energies below 8 MeV/nucleon, no theoretical model as such is available to explain ICF data satisfactorily. Different techniques have been employed for the study of ICF reactions such as: excitation function measurements of ERs, recoil range distributions of ERs, velocity distribution of ERs, kinetic energy spectra and angular distribution studies of PLFs, angular distribution measurement of the ERs and spin distribution measurements of ERs.

Most of the ICF reaction studies available in the literatures are confined to medium mass target nuclei and very few studies are available with heavier targets ($A > 150$). In the case of low and medium mass target nuclei, the ICF cross-section is a small fraction of the total fusion cross-section of the ERs. However, in case of heavier target nuclei, the α-particle(s) evaporation from the compound nucleus (CN) becomes less probable because of the high Coulomb barrier. Consequently, ICF cross-section associated with α-particle emission contributes the dominant component in the total fusion cross-section. In the present work an attempt has been made to address some of the important aspects of ICF reaction dynamics. With this aim EFs of eighteen ERs produced in the reaction of ^{20}Ne with ^{165}Ho have been measured in the energy range $\approx$ 4–8 MeV/nucleon. In the present measurement special care has been taken to remove the precursor decay contributions in the production of several ERs to get the direct production cross-sections of the residues. The measured EFs have been compared with the theoretical predictions of statistical model code PACE-2 [34], which takes into account only the CF process. The enhancement in the measured EFs for α-particle emission channels are interpreted in terms of ICF process. The dependence of ICF fraction with projectile energy has also been discussed. The entrance channel mass-asymmetry dependence on ICF fraction are also investigated and plotted along with the data available in the literature for other projectile-target systems: $^{20}\mathrm{Ne} + {}^{55}\mathrm{Mn}$

[24], $^{16}O + {}^{45}Sc$ [35,36], $^{20}Ne + {}^{59}Co$ [12] and $^{16}O + {}^{74}Ge$ [35,37]. A consistency has been observed and is discussed in Section 4. The present work is a part of ongoing program [11,12,24, 35–38] to study the CF and ICF dynamics in heavy ion induced reactions below 10 MeV/nucleon energies. To the best of our knowledge these measurements for the projectile-target system mentioned above have been reported for the first time and hence no data are available for comparison. However, it is worth to mention that present data well supports and supplement the recent findings [11] of forward recoil range distributions (RRDs) measurements of the ERs produced in the same projectile-target system at ≈ 8 MeV/nucleon.

2. Experimental details

The present experiments have been carried out using the heavy ion accelerator facility of the Variable Energy Cyclotron Centre (VECC), Kolkata, India. Stacked foil activation technique has been employed. One of the major advantages of stacked foil activation technique is that in a single irradiation many target foils are irradiated at different energies and large number of reactions may be studied. Details of target preparation, target–catcher irradiations, post irradiation analysis including energy and efficiency calibrations etc. are given in the following sections.

2.1. Target preparation

Self-supporting natural ^{165}Ho targets of desired thickness with purity better than (99.9%) were prepared by rolling machine at Saha Institute of Nuclear Physics (SINP) Target Lab, Kolkata, India. The thickness of each target foils was determined using microbalance as well as by α-particle transmission method, which is based on the measurement of the energy loss by 5.485 MeV α-particles obtained from ^{241}Am source, while passing through the target. Thickness of the holmium target foil was found to be ≈ 1.265 mg/cm^2. The targets were cut into size of 1.5×1.5 cm^2 each and were pasted on rectangular aluminum target holders having concentric holes of 1.2 cm diameter. The aluminum target holders were used for rapid heat dissipation.

2.2. Target irradiation

Two stacks of target-catcher assemblies were bombarded with the ^{20}Ne-ion beam in a specially designed vacuum chamber, shown elsewhere in our earlier Ref. [11], at Variable Energy Cyclotron Centre (VECC), Kolkata, India. The targets in the stack along with catcher foils were arranged in such a way that target material faced the beam, so that the recoiled residues may be trapped in the aluminum catchers. Aluminum-foils of thicknesses 1.2 and 0.8 mg/cm^2 kept between two successive ^{165}Ho targets that served as catchers as well as energy degraders, wherever desired. Two stacks consisting of six rolled holmium foils each of ^{165}Ho backed by thick aluminum foils were bombarded with an $^{20}Ne^{+7}$ beam energy ≈ 165 and 132 MeV. Two independent irradiations were carried out to encompass the beam energy ranging between 88–164 MeV. Weighted average beam current of ≈ 40 nA was measured behind the target assembly with an electron suppressed Faraday cup, using a current integrator device. Keeping in view the half-lives of interest, irradiations have been carried out for ≈ 8 hours duration for each stack. The mean energy of ^{20}Ne-ion beam at half the thickness on each foil in the stack was calculated from the energy degradation of the incident beam energy, using stopping power and range software

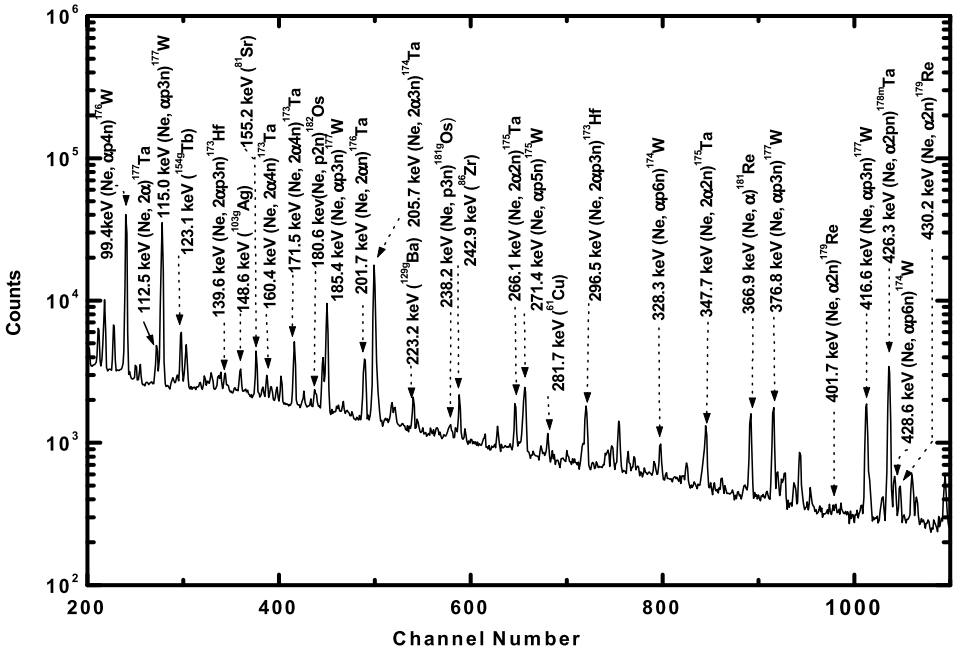

Fig. 1. Observed γ-ray energy spectrum of irradiated ^{165}Ho sample at 164 MeV ^{20}Ne-ion beam.

SRIM [39]. The inherent energy spread of 0.5 MeV has been reported in 165 MeV ^{20}Ne-ion beam. Moreover, when beam passes through the target and catcher foils, the energy spread due to straggling may come into picture. However, the energy spread due to straggling has not been considered due to its non-significant contribution [40].

2.3. Calibration of the HPGe detector and post-irradiation analysis

The measurement of the activity of ERs produced in a particular reaction is the most accurate way of measuring the cross-section of that residue. The off-beam measurements provide by far more accurate results not only because the background in γ-ray spectra is much smaller, but also because each residue may be identified both through the energy of its characteristic γ lines and its half-life by measuring the activity as a function of time. Details of energy and efficiency calibrations of the detector are given in Ref. [12]. Software packages MAESTRO [41] and FREEDOM [42] were used for recording and analysis of the data respectively. More over, the counting was carried out in live-time mode of the multichannel analyzer to incorporate the dead time loss. Typical γ-ray spectrum obtained from irradiated ^{165}Ho sample by 164 MeV ^{20}Ne-ion beam is shown in Fig. 2. The ERs were identified by their characteristic γ-rays as well as following their half-lives.

The experimentally measured reaction cross-section $\sigma_r(E)$, for a particular reaction product has been computed using the following expression given in Ref. [43].

$$\sigma_r(E) = \frac{A\lambda \exp(\lambda t_2)}{N_0 \phi \vartheta \varepsilon_G K [1 - \exp(-\lambda t_1)][1 - \exp(-\lambda t_3)]} \tag{1}$$

Table 1
List of reactions, identified γ-rays and their branching ratios for the system ^{20}Ne + ^{165}Ho.

S. No.	Reactions	Half-life	E_γ (keV)	Branching ratio, θ(%)
1.	^{165}Ho(Ne, 3n)^{182}Ir	15.00 m	126.2[a]	34.4
2.	^{165}Ho(Ne, p2n)^{182}Os	21.60 h	180.6[a]	34.7
3.	^{165}Ho(Ne, p3n)^{181g}Os	1.75 h	238.2[a]	44.0
			826.7	20.0
4.	^{165}Ho(Ne, α)^{181}Re	19.90 h	366.9[a]	57.0
5.	^{165}Ho(Ne, α2n)^{179}Re	19.70 m	401.7	7.2
			430.2[a]	28.0
6.	^{165}Ho(Ne, α3n)^{178}Re	13.20 m	105.3[a]	23.1
7.	^{165}Ho(Ne, α4n)^{177}Re	14.00 m	196.4[a]	8.4
8.	^{165}Ho(Ne, αp3n)^{177}W	2.21 h	115.0[a]	59.0
			185.4[a]	16.1
			376.8	4.6
			416.6	6.1
			1036.9	10.2
9.	^{165}Ho(Ne, αp4n)^{176}W	2.50 h	99.4[a]	73.0
10.	^{165}Ho(Ne, αp6n)^{174}W	29.00 m	328.3	9.5
			428.6[a]	12.7
11.	^{165}Ho(Ne, α2pn)^{178m}Ta	2.50 h	426.3[a]	97.1
12.	^{165}Ho(Ne, 2α)^{177}Ta	56.60 h	112.5[a]	7.2
13.	^{165}Ho(Ne, 2αn)^{176}Ta	8.10 h	201.7[a]	5.5
			710.5	5.2
14.	^{165}Ho(Ne, 2α2n)^{175}Ta	10.50 h	266.1[a]	10.3
			347.7	11.4
15.	^{165}Ho(Ne, 2α3n)^{174}Ta	1.18 h	90.9	15.9
			205.7[a]	57.7
16.	^{165}Ho(Ne, 2α4n)^{173}Ta	3.65 h	160.4	4.8
			171.5[a]	17.0
17.	^{165}Ho(Ne, 2αp3n)^{173}Hf	23.60 h	139.6	12.4
			296.5[a]	33.9
18.	^{165}Ho(Ne, 4α3n)^{166}Tm	7.70 h	691.2	7.4
			778.4[a]	15.1

[a] γ-Lines used for experimental data analysis.

where, A is the total number of counts observed under the photo-peak of characteristic γ-ray in time t_3, λ is decay constant of the residual nucleus, N_0 is the total number of nuclei present in the target, ϕ is the incident ion beam flux, θ is the branching ratio of identified γ-ray, ε_G is the geometry dependent efficiency of the detector, t_1 is the irradiation time, t_2 is the time lapse between end of irradiation and start of counting and t_3 in the data collection time, $K = [1 - \exp(-\mu d)]/\mu d$ is the correction for self-absorption of the γ-ray in the sample itself, with absorption coefficient μ for the target of thickness 'd'. A factor $[1 - \exp(-\lambda t_1)]$ takes care of the decay of evaporation residue during irradiation time 't_1' and is known as the 'saturation correction factor'. The correction factor for the decay of the induced activity due to delay time 't_2' between stop of irradiation and the start of counting is taken care of by $[\exp(-\lambda t_2)]$ and the correction factor due to the decay of irradiated sample during data accumulation time 't_3' is taken as $[1 - \exp(-\lambda t_3)]$. The characteristic γ-ray energies, their abundances and half-lives of the ERs etc. are taken from Table of Isotopes [44]. The spectroscopic data used for yield calculations are listed in Table 1.

3. Extraction of direct cross-sections from the measured cumulative cross-sections

In the interaction of ^{20}Ne with the target nucleus ^{165}Ho, it has been observed that the some of the ERs may be produced both directly as well as by decay of the produced higher Z precursor isobars through β^+-emission, and/or EC. For such cases, cumulative cross-sections have been measured, if the half-life of the precursor is considerably smaller than that of the evaporation residue. Both directly produced and in precursor decay, gives a cross-section, which is the sum of the production cross-section of the observed residue and the cross-sections for production of its precursors multiplied by a numerical coefficient P_P. This coefficient may be greater than unity and depend both on the branching ratios for the decay of the precursors to the evaporation residue considered and on the half-lives of the precursor and the evaporation residue. An attempt has been made to separate out the contribution from precursor decay by using the prescription of Cavinato et al. [20]. For the isobaric decay of parent P to daughter D, i.e. $P \rightarrow D$, the cumulative cross-section of the daughter nucleus is given by,

$$\sigma^D_{cum} = \sigma^D_{dir} + P_P \frac{T^D_{1/2}}{T^D_{1/2} - T^P_{1/2}} \sigma^P_{dir} \tag{2}$$

where $T^P_{1/2}$ and $T^D_{1/2}$ are the half-life of parent and daughter nuclei, P_P is the branching intensity, σ^D_{cum} is the cumulative cross-section of the daughter nucleus, σ^D_{dir} is the direct cross-section of the daughter nucleus and σ^P_{dir} is the direct cross-section of the parent nucleus production. This procedure has been generalized to the case of successive decay of several precursor isobars produced in addition to the direct production of the residue. In case of decay of two precursor isobars A and B, produced in the beam interaction, that is,

$$A \rightarrow B \rightarrow C$$

with half-lives $T^A_{1/2} \ll T^B_{1/2} \ll T^C_{1/2}$ and with branching ratios P_A and P_B, the cumulative cross-section for the production of the residue C has been obtained as [20],

$$\sigma^C_{cum} = \sigma^C_{dir} + P_B \frac{T^C_{1/2}}{(T^C_{1/2} - T^B_{1/2})} \sigma^B_{dir} + P_A P_B \frac{(T^C_{1/2})^2}{(T^C_{1/2} - T^A_{1/2})(T^C_{1/2} - T^B_{1/2})} \sigma^A_{dir} \tag{3}$$

The contribution of the precursor decay has been separated out from measured cumulative cross-section to deduce the direct cross-section of a reaction by using Eqs. (2) and (3).

As an example, ^{182}Os may be produced by two routes, namely, ^{182}Os (p2n) as well as ^{182}Ir (3n) followed by EC/β^+ decay of ^{182}Ir. The cumulative cross-section of ^{182}Os has been measured by following the γ-ray activities at times longer than about 6–8 half-lives of the precursor, so that precursor completely decayed to ^{182}Os. The residual nucleus, ^{182}Os decays to ^{182}Re by EC and has been identified by 180.6 keV γ-ray. The direct cross-sections from the measured cumulative cross-sections for the production of ^{182}Os separated by using the Cavinato et al. [20] formulation based expression (2)

$$\sigma^{meas}_{cum}\left(^{182}\text{Os}\right) = \sigma^{meas}_{dir}\left(^{182}\text{Os}\right) + 1.012\sigma^{meas}_{dir}\left(^{182}\text{Ir}\right) \tag{4}$$

where $\sigma^{meas}_{dir}(^{182}\text{Ir})$ is the direct cross-section of the precursor ^{182}Ir, whose contributions have been subtracted from the cumulative cross-section $\sigma^{meas}_{cum}(^{182}\text{Os})$ to obtain the direct cross-section of residue ^{182}Os as $\sigma^{meas}_{dir}(^{182}\text{Os})$ at each projectile energy.

Similarly, ^{181}Re may be produced either by ^{181}Ir (4n) or ^{181}Os (p3n) followed by isobaric decay to ^{181}Re. In this case, the cumulative cross-section of ^{181}Re measured after 6–8 half-lives of precursors may have contributions from the decay of precursor isobars ^{181}Ir and ^{181}Os in addition to the direct production of ^{181}Re. The measured cumulative cross-section of its precursor ^{181g}Os has been separated from its measured cumulative cross-section of ^{181}Re to get the direct cross-section for the production of ^{181}Re using expression (2). In the present case the expression reduces to the form:

$$\sigma_{cum}^{meas}\left(^{181}\mathrm{Re}\right) = \sigma_{dir}^{meas}\left(^{181}\mathrm{Re}\right) + 1.096\sigma_{cum}^{meas}\left(^{181g}\mathrm{Os}\right) \tag{5}$$

where $\sigma_{cum}^{meas}(^{181g}\mathrm{Os})$ is the cumulative cross-section of the precursor ^{181}Os, which contributions have been subtracted from the cumulative cross-section $\sigma_{cum}^{meas}(^{181}\mathrm{Re})$ to obtain its direct production cross-section $\sigma_{dir}^{meas}(^{181}\mathrm{Re})$ at each projectile energy. This case needs special attention as the measured cross-section for ^{181}Os corresponds to only ground state with half-life 1.75 hrs. Since, the metastable state (half-life 2.7 min) contribution could not be measured, the deduced direct cross-sections for the production of ^{181}Re is expected to be a little less than whatever deduced.

In the case of $^{177-179}$Re, the αxn channels may have contribution from ICF involving break-up of ^{20}Ne into $^{16}\mathrm{O} + \alpha$ followed by fusion of ^{16}O with the target nucleus giving ^{181}Re as the incompletely fused composite nucleus which may subsequently de-excite by neutron emission to yield the Re isotopes. As such, measured cross-sections include contributions from CF and ICF processes. To study this reaction we have followed the of 196.4 keV γ-ray in the decay of the product nucleus ^{177}Re. The residue ^{177}Re produced via the reaction ^{177}Re (α4n) may also be populated by EC and/or β^+ decay of the higher charge precursor isobars i.e. ^{177}Ir and ^{177}Os produced in 8n and p7n emission channels respectively. The measured cumulative cross-section of ^{177}Re has contributions from the decay of precursor isobars ^{177}Ir (30 sec) and ^{177}Os (2.8 min) produced in addition to direct production of ^{177}Re. For cumulative cross-section measurement, the induced γ-ray activities have been measured after the complete decay of the precursor ^{177}Os to the residue ^{177}Re. The direct cross-section for the production of ^{177}Re has been deduced from the measured cumulative cross-section using expression (3). In the present case the expression reduces to the form:

$$\sigma_{cum}^{meas}\left(^{177}\mathrm{Re}\right) = \sigma_{dir}^{meas}\left(^{177}\mathrm{Re}\right) + 1.250\sigma_{dir}^{PACE}\left(^{177}\mathrm{Os}\right) + 1.296\sigma_{dir}^{PACE}\left(^{177}\mathrm{Ir}\right) \tag{6}$$

where $\sigma_{dir}^{PACE}(^{177}\mathrm{Ir})$ and $\sigma_{dir}^{PACE}(^{177}\mathrm{Os})$ are the direct cross-sections of the precursors ^{177}Ir and ^{177}Os respectively. Their contributions have been subtracted from the cumulative cross-section $\sigma_{cum}^{meas}(^{177}\mathrm{Re})$ to obtain direct production cross-section $\sigma_{dir}^{meas}(^{177}\mathrm{Re})$ at each projectile energy.

In the similar way, the direct production cross-sections for the ERs ^{181g}Os (p3n), ^{179}Re (α2n), ^{178}Re (α3n), ^{177}W (αp3n), ^{177}Ta (2α), ^{176}Ta (2αn), ^{174}Ta (2α3n) and ^{173}Hf (2αp3n) have also been deduced from the measured cumulative cross-sections and their precursor contributions by using expressions based on Cavinato et al. [20] formulation, given in Table 2.

Many factors are responsible for the errors and uncertainty in the experimentally measured cross-sections. These are the uncertainty in the determination of the efficiency of the HPGe detector, errors in the flux measurement due to the fluctuation in beam current, uncertainty in the determination of thickness of the target due to non-uniformity in the target, The overall errors from all these factors including statistical errors in the photo-peak area are estimated. The errors associated with the spectroscopic data like branching intensity and half-life of the product nuclei have not been taken into account, because any revision in the spectroscopic data would permit an easy re-calculation of the cross-section in future. The detailed discussion of the error analysis

Table 2
Deduced expressions used for extraction of direct cross-sections from the measured cumulative cross-sections.

Residues	Measured cross-section	Expressions used for extraction of direct production cross-sections
^{182}Os	Direct yield	$\sigma_{cum}^{meas}(^{182}\mathrm{Os}) = \sigma_{dir}^{meas}(^{182}\mathrm{Os}) + 1.012\sigma_{dir}^{meas}(^{182}\mathrm{Ir})$
^{181g}Os	Direct yield	$\sigma_{cum}^{meas}(^{181g}\mathrm{Os}) = \sigma_{dir}^{meas}(^{181g}\mathrm{Os}) + 1.049\sigma_{dir}^{PACE}(^{181}\mathrm{Ir})$
^{181}Re	Direct yield	$\sigma_{cum}^{meas}(^{181}\mathrm{Re}) = \sigma_{dir}^{meas}(^{181}\mathrm{Re}) + 1.096\sigma_{cum}^{meas}(^{181g}\mathrm{Os})$
^{179}Re	Direct yield	$\sigma_{cum}^{meas}(^{179}\mathrm{Re}) = \sigma_{dir}^{meas}(^{179}\mathrm{Re}) + 1.492\sigma_{dir}^{PACE}(^{179}\mathrm{Os}) + 1.600\sigma_{dir}^{PACE}(^{179}\mathrm{Ir})$
^{178}Re	Direct yield	$\sigma_{cum}^{meas}(^{178}\mathrm{Re}) = \sigma_{dir}^{meas}(^{178}\mathrm{Re}) + 1.610\sigma_{dir}^{PACE}(^{178}\mathrm{Os}) + 1.634\sigma_{dir}^{PACE}(^{178}\mathrm{Ir})$
^{177}Re	Direct yield	$\sigma_{cum}^{meas}(^{177}\mathrm{Re}) = \sigma_{dir}^{meas}(^{177}\mathrm{Re}) + 1.250\sigma_{dir}^{PACE}(^{177}\mathrm{Os}) + 1.296\sigma_{dir}^{PACE}(^{177}\mathrm{Ir})$
^{177}W	Direct yield	$\sigma_{cum}^{meas}(^{177}\mathrm{W}) = \sigma_{dir}^{meas}(^{177}\mathrm{W}) + 1.118\sigma_{cum}^{meas}(^{177}\mathrm{Re})$
^{177}Ta	Direct yield	$\sigma_{cum}^{meas}(^{177}\mathrm{Ta}) = \sigma_{dir}^{meas}(^{177}\mathrm{Ta}) + 1.041\sigma_{cum}^{meas}(^{177}\mathrm{W})$
^{176}Ta	Direct yield	$\sigma_{cum}^{meas}(^{176}\mathrm{Ta}) = \sigma_{dir}^{meas}(^{176}\mathrm{Ta}) + 1.446\sigma_{cum}^{meas}(^{176}\mathrm{W})$
^{174}Ta	Direct yield	$\sigma_{cum}^{meas}(^{174}\mathrm{Ta}) = \sigma_{dir}^{meas}(^{174}\mathrm{Ta}) + 1.686\sigma_{cum}^{meas}(^{174}\mathrm{W})$
^{173}Hf	Direct yield	$\sigma_{cum}^{meas}(^{173}\mathrm{Hf}) = \sigma_{dir}^{meas}(^{173}\mathrm{Hf}) + 1.153\sigma_{cum}^{meas}(^{173}\mathrm{Ta})$

Table 3
Experimentally measured cross-sections for the production of the evaporation residues ^{182}Ir, ^{182}Os and ^{181g}Os.

$E_{lab} \pm \Delta E$ (MeV)	σ_{dir} (^{182}Ir) (mb)	σ_{cum} (^{182}Os) (mb)	σ_{dir} (^{182}Os) (mb)	σ_{cum} (^{181g}Os) (mb)	σ_{dir} (^{181g}Os) (mb)
88.5 ± 2.3	–	–	–	2.7 ± 0.2	0.7 ± 0.2
96.0 ± 2.2	5.0 ± 1.2	6.2 ± 0.7	1.2 ± 0.2	176.5 ± 8.0	12.9 ± 8.0
103.0 ± 2.1	1.9 ± 0.4	3.9 ± 0.4	1.9 ± 0.4	213.8 ± 10.3	18.0 ± 10.3
110.0 ± 2.1	0.4 ± 0.1	1.1 ± 0.1	0.6 ± 0.1	120.0 ± 10.7	20.0 ± 10.7
117.1 ± 2.1	–	0.3 ± 0.04	0.2 ± 0.05	51.2 ± 5.1	17.2 ± 5.1
123.7 ± 2.0	–	0.1 ± 0.01	0.1 ± 0.03	11.5 ± 1.4	3.8 ± 1.4
130.1 ± 2.0	–	–	–	1.3 ± 0.1	0.3 ± 0.1
134.1 ± 2.0	–	–	–	0.9 ± 0.2	0.5 ± 0.2
141.8 ± 1.9	–	–	–	0.2 ± 0.05	0.1 ± 0.05
149.3 ± 1.9	–	–	–	0.1 ± 0.05	0.1 ± 0.05
156.5 ± 1.9	–	–	–	0.1 ± 0.05	0.1 ± 0.05

has been given in our earlier Ref. [36]. Experimentally measured cross-sections (direct and cumulative) for the production of various ERs obtained for different ^{20}Ne-ion beam energy along with the estimated errors are tabulated in Tables 3–7. The details of theoretical calculations and the parameters used are discussed in the following section.

4. Analysis of the experimental data

4.1. EFs analysis with code PACE-2

In general, it has been assumed that most of the decay properties of the excited nuclei produced in HI reactions can be described by statistical model calculations. The theoretical estimates of the reaction cross-sections were made by the code PACE-2 [34]. The code PACE-2 is based on the statistical model approach and uses the Monte Carlo simulation procedure for the de-excitation of compound nucleus. The angular momentum projections are calculated at each stage of de-excitation, which enables to determine the angular distribution of emitted particles. The

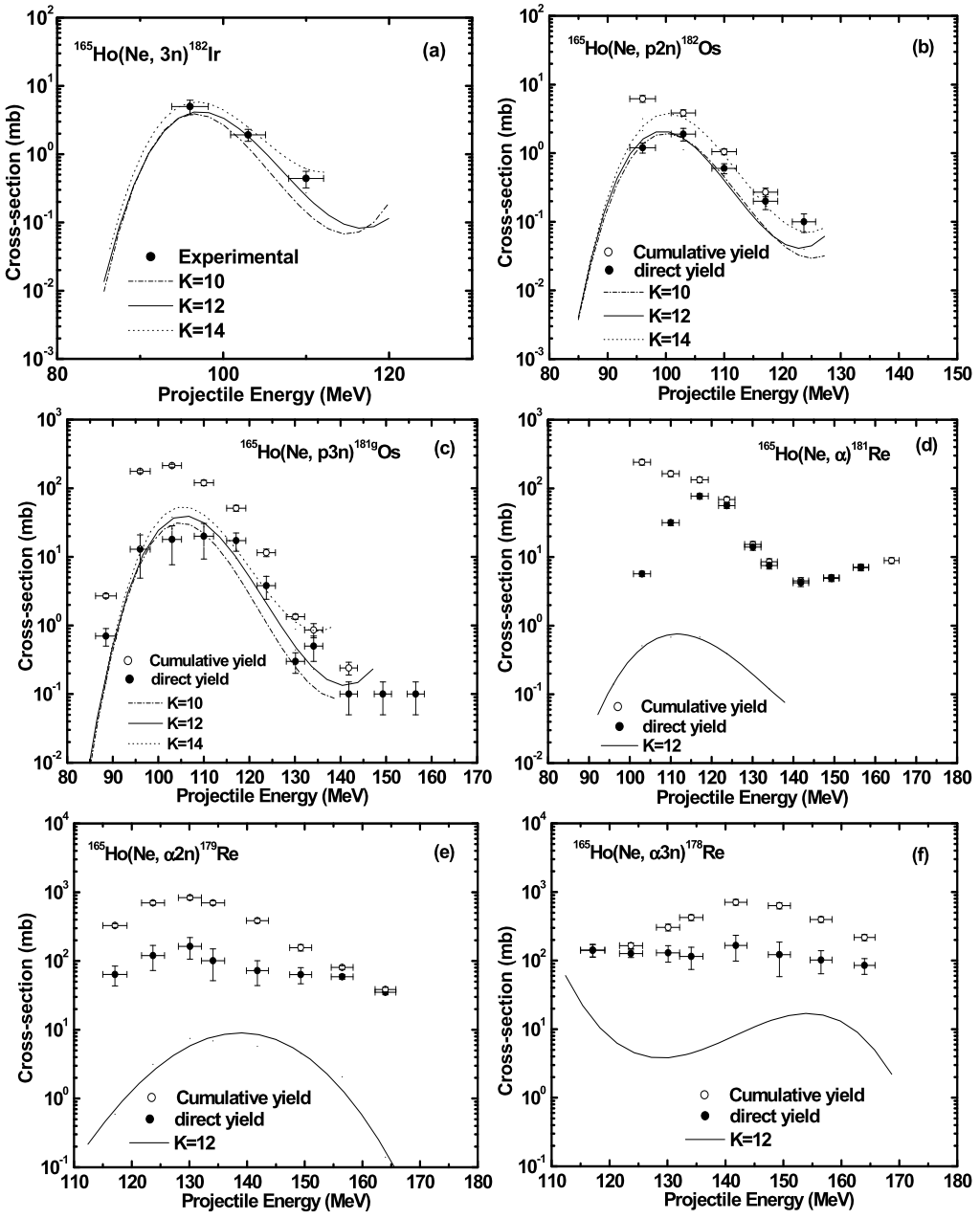

Fig. 2. (a)–(c) Excitation functions of the ERs produced in ^{20}Ne + ^{165}Ho reaction. Solid circles represent experimental data. The solid, dotted and dash dotted lines correspond to the theoretical predictions of PACE-2 for different values of level density parameter constant K. In (b)–(f) open circles represent the cumulative yield for the production of residue ^{182}Os, ^{181g}Os, ^{181}Re, ^{179}Re, ^{178}Re and solid circles represent its measured direct yield. Solid lines correspond to PACE-2 predictions corresponding to $K = 12$.

Table 4
Experimentally measured cross-sections for the production of the evaporation residues ^{181}Re, ^{179}Re and ^{178}Re.

$E_{lab} \pm \Delta E$ (MeV)	$\sigma_{cum}(^{181}\mathrm{Re})$ (mb)	$\sigma_{dir}(^{181}\mathrm{Re})$ (mb)	$\sigma_{cum}(^{179}\mathrm{Re})$ (mb)	$\sigma_{dir}(^{179}\mathrm{Re})$ (mb)	$\sigma_{cum}(^{178}\mathrm{Re})$ (mb)	$\sigma_{dir}(^{178}\mathrm{Re})$ (mb)
103.0 ± 2.1	240.1 ± 22.6	5.7 ± 0.5	–	–	–	–
110.0 ± 2.1	163.2 ± 15.4	31.6 ± 3.0	–	–	–	–
117.1 ± 2.1	132.9 ± 12.6	76.8 ± 7.2	327.6 ± 20.4	63.9 ± 20.4	142.3 ± 29.4	141.2 ± 29.4
123.7 ± 2.0	68.6 ± 6.5	56.0 ± 5.3	698.5 ± 47.3	120.2 ± 47.3	164.5 ± 15.9	126.9 ± 15.9
130.1 ± 2.0	15.3 ± 1.5	13.9 ± 1.4	831.9 ± 56.2	162.7 ± 56.2	304.8 ± 34.9	130.0 ± 34.9
134.1 ± 2.0	8.5 ± 0.9	7.5 ± 0.8	701.2 ± 49.3	100.9 ± 49.3	424.2 ± 41.1	114.5 ± 41.1
141.8 ± 1.9	4.5 ± 0.5	4.2 ± 0.5	384.8 ± 28.3	72.2 ± 28.3	710.0 ± 67.5	165.4 ± 67.5
149.3 ± 1.9	5.0 ± 0.5	4.9 ± 0.5	156.4 ± 16.6	63.3 ± 16.6	630.0 ± 63.9	120.2 ± 63.9
156.5 ± 1.9	7.1 ± 0.7	7.0 ± 0.7	80.4 ± 4.7	59.0 ± 4.7	398.0 ± 37.8	102.0 ± 37.8
164.0 ± 1.8	8.9 ± 0.9	–	38.4 ± 2.8	35.1 ± 2.8	217.0 ± 22.0	84.4 ± 22.0

Table 5
Experimentally measured cross-sections for the production of the evaporation residues ^{177}Re, ^{177}W, ^{176}W and ^{174}W.

$E_{lab} \pm \Delta E$ (MeV)	$\sigma_{cum}(^{177}\mathrm{Re})$ (mb)	$\sigma_{dir}(^{177}\mathrm{Re})$ (mb)	$\sigma_{cum}(^{177}\mathrm{W})$ (mb)	$\sigma_{dir}(^{177}\mathrm{W})$ (mb)	$\sigma_{cum}(^{176}\mathrm{W})$ (mb)	$\sigma_{cum}(^{174}\mathrm{W})$ (mb)
103.0 ± 2.1	99.9 ± 16.9	–	–	–	0.8 ± 0.1	–
110.0 ± 2.1	139.8 ± 26.1	–	172.8 ± 13.0	16.5 ± 1.2	4.5 ± 0.5	–
117.1 ± 2.1	124.8 ± 24.5	–	207.5 ± 6.0	68.0 ± 2.0	23.4 ± 2.3	–
123.7 ± 2.0	67.0 ± 9.7	–	168.5 ± 4.9	93.6 ± 2.7	20.9 ± 2.0	33.2 ± 4.8
130.1 ± 2.0	118.8 ± 12.0	118.4 ± 12.0	210.3 ± 8.0	77.5 ± 2.9	31.4 ± 2.3	70.0 ± 5.7
134.1 ± 2.0	91.5 ± 9.8	87.2 ± 9.8	215.1 ± 5.4	112.8 ± 2.8	66.6 ± 3.6	99.1 ± 9.4
141.8 ± 1.9	121.7 ± 16.0	76.3 ± 16.0	238.1 ± 5.6	102.0 ± 2.4	56.3 ± 3.1	90.9 ± 6.8
149.3 ± 1.9	289.9 ± 59.0	118.8 ± 59.0	389.6 ± 12.3	65.5 ± 2.1	53.8 ± 5.1	104.1 ± 12.7
156.5 ± 1.9	434.9 ± 43.9	166.6 ± 43.9	519.2 ± 12.3	32.9 ± 0.8	60.8 ± 4.1	210.0 ± 17.9
164.0 ± 1.8	328.8 ± 38.9	121.5 ± 38.9	778.6 ± 21.0	350.6 ± 9.4	86.7 ± 6.1	254.8 ± 19.3

CF cross-sections are calculated using Bass formula [45]. The partial reaction cross-section for the formation of the compound nucleus at particular value of the angular momentum and specific bombarding energy, E is given by

$$\sigma_\ell = \pi \lambda\!\!\!^{-2} (2\ell + 1) T_\ell \tag{7}$$

where $\lambda\!\!\!^{-}$ is the de Broglie wavelength, and transmission coefficient (T_ℓ) is taken to be

$$T_\ell = \left[1 + \exp\left(\frac{\ell - \ell_{\max}}{\Delta} \right) \right]^{-1} \tag{8}$$

where Δ is the diffuseness parameter and $\ell_{\max}$ is determined by the total CF cross-section,

$$\sigma_F = \sum_{\ell}^{\infty} \sigma_\ell \tag{9}$$

The transmission coefficient for light particles n, p and α emission were determined using optical model potentials. The γ-ray strength functions, required for $E1$, $E2$, and $M1$ transition were taken from Tables of Endt [46]. In this code masses are read from the Atomic Mass Table [47] and if the table does not contain mass, rotating liquid drop mass due to Lysekil is substituted. Fission is considered as a decay mode, while the ICF is not taken into account in PACE-2 calculations

Table 6
Experimentally measured cross-sections for the production of the evaporation residues ^{178m}Ta, ^{177}Ta, ^{176}Ta and ^{175}Ta.

$E_{lab} \pm \Delta E$ (MeV)	$\sigma_{dir}(^{178m}\text{Ta})$ (mb)	$\sigma_{cum}(^{177}\text{Ta})$ (mb)	$\sigma_{dir}(^{177}\text{Ta})$ (mb)	$\sigma_{cum}(^{176}\text{Ta})$ (mb)	$\sigma_{dir}(^{176}\text{Ta})$ (mb)	$\sigma_{cum}(^{175}\text{Ta})$ (mb)
88.5 ± 2.3	–	8.2 ± 1.6	–	–	–	–
96.0 ± 2.2	–	7.2 ± 1.2	–	–	–	2.2 ± 0.9
103.0 ± 2.1	–	29.9 ± 3.8	–	–	–	3.7 ± 0.4
110.0 ± 2.1	–	185.2 ± 18.0	5.3 ± 0.5	8.8 ± 2.2	2.3 ± 0.2	11.5 ± 2.5
117.1 ± 2.1	3.2 ± 0.3	224.1 ± 23.9	8.1 ± 0.9	46.6 ± 11.6	12.7 ± 3.2	39.3 ± 9.9
123.7 ± 2.0	7.2 ± 0.5	227.8 ± 24.5	52.3 ± 5.6	50.6 ± 12.6	20.3 ± 5.1	29.7 ± 5.0
130.1 ± 2.0	5.1 ± 1.0	291.9 ± 32.0	72.8 ± 8.0	88.5 ± 22.1	43.1 ± 10.8	61.8 ± 5.9
134.1 ± 2.0	5.5 ± 0.5	286.0 ± 27.4	62.0 ± 5.9	145.3 ± 11.7	48.9 ± 3.9	96.3 ± 4.7
141.8 ± 1.9	14.2 ± 1.1	332.4 ± 29.6	84.5 ± 7.5	173.8 ± 27.3	92.4 ± 14.5	192.3 ± 9.2
149.3 ± 1.9	20.4 ± 1.1	639.2 ± 60.5	233.2 ± 22.1	178.6 ± 17.3	100.8 ± 10.0	247.7 ± 13.7
156.5 ± 1.9	23.1 ± 1.4	756.7 ± 71.7	216.0 ± 20.4	180.1 ± 18.8	92.2 ± 9.6	336.4 ± 16.4
164.0 ± 1.8	21.1 ± 1.2	905.3 ± 86.7	94.5 ± 9.1	237.9 ± 19.5	112.4 ± 9.2	261.2 ± 12.9

Table 7
Experimentally measured cross-sections for the production of the evaporation residues ^{174}Ta, ^{173}Ta, ^{173}Hf and ^{166}Tm.

$E_{lab} \pm \Delta E$ (MeV)	$\sigma_{cum}(^{174}\text{Ta})$ (mb)	$\sigma_{dir}(^{174}\text{Ta})$ (mb)	$\sigma_{cum}(^{173}\text{Ta})$ (mb)	$\sigma_{cum}(^{173}\text{Hf})$ (mb)	$\sigma_{dir}(^{173}\text{Hf})$ (mb)	$\sigma_{dir}(^{166}\text{Tm})$ (mb)
96.0 ± 2.2	–	–		0.5 ± 0.1	–	–
103.0 ± 2.1	–	–	–	0.8 ± 0.1	–	5.6 ± 1.0
110.0 ± 2.1	2.97 ± 0.3	–	–	3.2 ± 0.3	–	10.4 ± 2.0
117.1 ± 2.1	22.9 ± 2.4	–	–	2.2 ± 0.2	–	21.6 ± 1.9
123.7 ± 2.0	65.4 ± 6.3	9.4 ± 2.3	–	4.6 ± 0.4	–	31.6 ± 3.9
130.1 ± 2.0	201.5 ± 19.7	83.4 ± 13.0	5.8 ± 0.6	10.6 ± 1.0	3.9 ± 0.4	54.4 ± 6.3
134.1 ± 2.0	336.9 ± 70.6	169.9 ± 42.3	7.1 ± 0.6	16.6 ± 1.2	8.5 ± 0.6	51.9 ± 5.8
141.8 ± 1.9	340.6 ± 103.5	187.3 ± 64.0	8.8 ± 0.9	23.1 ± 1.6	13.0 ± 0.9	67.1 ± 4.5
149.3 ± 1.9	284.3 ± 27.0	108.7 ± 13.7	9.7 ± 0.7	24.7 ± 2.4	13.5 ± 1.3	63.7 ± 3.6
156.5 ± 1.9	445.3 ± 48.8	91.3 ± 23.0	23.2 ± 1.4	48.6 ± 3.3	22.0 ± 1.5	55.8 ± 4.9
164.0 ± 1.8	553.1 ± 55.9	123.7 ± 49.1	47.5 ± 2.6	79.2 ± 5.7	24.6 ± 1.8	66.3 ± 3.9

and hence the enhancement, if found, in the measured excitation functions (EF) over PACE-2 predictions, for the residues that are produced in the break-up of projectile into α-clusters, may be attributed to the ICF process. The rotational energy of the decaying nuclei was calculated using the rotating liquid drop model with diffused surface. In the present calculations of EFs for ERs, the value of level density parameter 'a' was calculated using the relation $a = A/K$ MeV^{-1}, where 'A' is the mass number of the residual nucleus and 'K' is called level density parameter constant, which affects the equilibrium components. Owing to the high emission barrier for the charged particles in the exit channel, the emission of protons and alpha particles from the CN is hindered resulting in much lower cross-section for the pxn (x = 1, 2, 3, ...) and αxn (x = 1, 2, 3, ...) ERs in CF. Consequently any ICF process is reflected in the enhanced cross-sections of these ERs. Of course, the PACE-2 code does give the cross-section of ERs formed in alpha as well 2p emission processes, which have been taken into consideration during the CF cross-section calculation. In this code the most of required input parameters have been used as default except the charge and mass of the projectile and target nucleus.

4.2. Interpretation of the experimental results

The EFs for the eighteen ERs ^{182}Ir (3n), ^{182}Os (p2n), ^{181}Os (p3n), ^{181}Re (α), ^{179}Re (α2n), ^{178}Re (α3n), ^{177}Re (α4n), ^{177}W (αp3n), ^{176}W (αp4n), ^{174}W (αp6n), ^{178m}Ta (α2pn), ^{177}Ta (2α), ^{176}Ta (2αn), ^{175}Ta (2α2n), ^{174}Ta (2α3n), ^{173}Ta (2α4n), ^{173}Hf (2αp3n) and ^{166}Tm (4α3n) produced in the interaction of ^{20}Ne with ^{165}Ho are measured between 88–164 MeV projectile energy. The experimentally measured and theoretically calculated EFs for these eighteen ERs are displayed in Figs. 2–4. The excitation function (EF) for ER ^{182}Ir produced in the reaction ^{182}Ir (3n), is measured directly and is shown in Fig. 2(a). Cumulative cross-sections for ^{182}Os are measured after the complete decay of its precursor ^{182}Ir into ^{182}Os. Direct cross-section of ^{182}Os has been obtained by correcting for the contribution from precursor decay using the expression listed in Table 2. The direct cross-sections for the evaporation residue ^{181g}Os has also been deduced by correcting for the contributions of the decay of produced higher Z precursor isobar ^{181}Ir into ^{181}Os from the measured cumulative cross-sections of ^{181}Os, after the complete decay of its precursor ^{181}Ir by EC process, using the expressions given in Table 2. The effect of variation of 'K' (= 10, 12, 14) on the calculated EFs for the ERs produced in the reactions ^{182}Ir (3n), ^{182}Os (p2n) and ^{181g}Os (p3n) are shown in Figs. 2(a), 2(b) and 2(c) respectively. It is quite clear from these figures that PACE-2 predictions corresponding to $K = 12$ reproduce the measured EFs satisfactorily and these reaction channels are populated via CF process. The production detail of the ER ^{182}Ir is shown by the following reaction equations.

The evaporation residue ^{182}Ir is populated via CF of ^{20}Ne with ^{165}Ho,

$$^{20}\mathrm{Ne} + {}^{165}\mathrm{Ho} \rightarrow {}^{185}\mathrm{Ir}^{*} \rightarrow {}^{182}\mathrm{Ir} + 3\mathrm{n}$$

Similarly, the evaporation residue ^{182}Os produced in CF process may be populated via two different reaction modes as follows.

(i) CF of ^{20}Ne with ^{165}Ho i.e.

$$^{20}\mathrm{Ne} + {}^{165}\mathrm{Ho} \rightarrow {}^{185}\mathrm{Ir}^{*} \rightarrow {}^{182}\mathrm{Os} + \mathrm{p} + 2\mathrm{n}$$

(ii) Through the EC/β^{+}-decay of higher Z precursor isobar,

$$^{20}\mathrm{Ne} + {}^{165}\mathrm{Ho} \rightarrow {}^{182}\mathrm{Ir}^{*} + 3\mathrm{n}$$

$$^{182}\mathrm{Ir}^{*} \rightarrow {}^{182}\mathrm{Os} + \mathrm{EC}/\beta^{+}$$

As such, the evaporation residue ^{181}Os may also be populated via two different reaction modes.

The ERs produced in the reactions ^{181}Re (α), ^{179}Re (α2n), ^{178}Re (α3n), ^{177}Re (α4n) and ^{177}W (αp3n) may also populated by the decay of their higher charge precursor isobars in addition to the direct production of these ERs. The contribution due to the decay of higher Z precursor isobars to these ERs has been separated from measured cumulative cross-section to get the direct cross-section for the production of these ERs by using the expressions given in Table 2. The direct cross-sections for the production of evaporation residue ^{181}Re ^{179}Re, ^{178}Re, ^{177}Re and ^{177}W compared with PACE-2 calculated values, as shown in Figs. 2(d)–(f) and 3(a)–(b), it is observed that the measured direct EFs are much enhanced over their theoretical values. Since ICF is not considered in PACE-2 calculations, this enhancement may be attributed to the fact that this channel may be populated not only by CF of ^{20}Ne but may also have a significant contribution from ICF of ^{20}Ne i.e. fusion of fragment ^{16}O with the target ^{165}Ho (if ^{20}Ne breaks up into α and ^{16}O fragments). The evaporation residue ^{181}Re is predominantly formed by EC decay of precursors ^{181}Ir (4n) and ^{181}Os (p3n) products which have shorter half lives than the

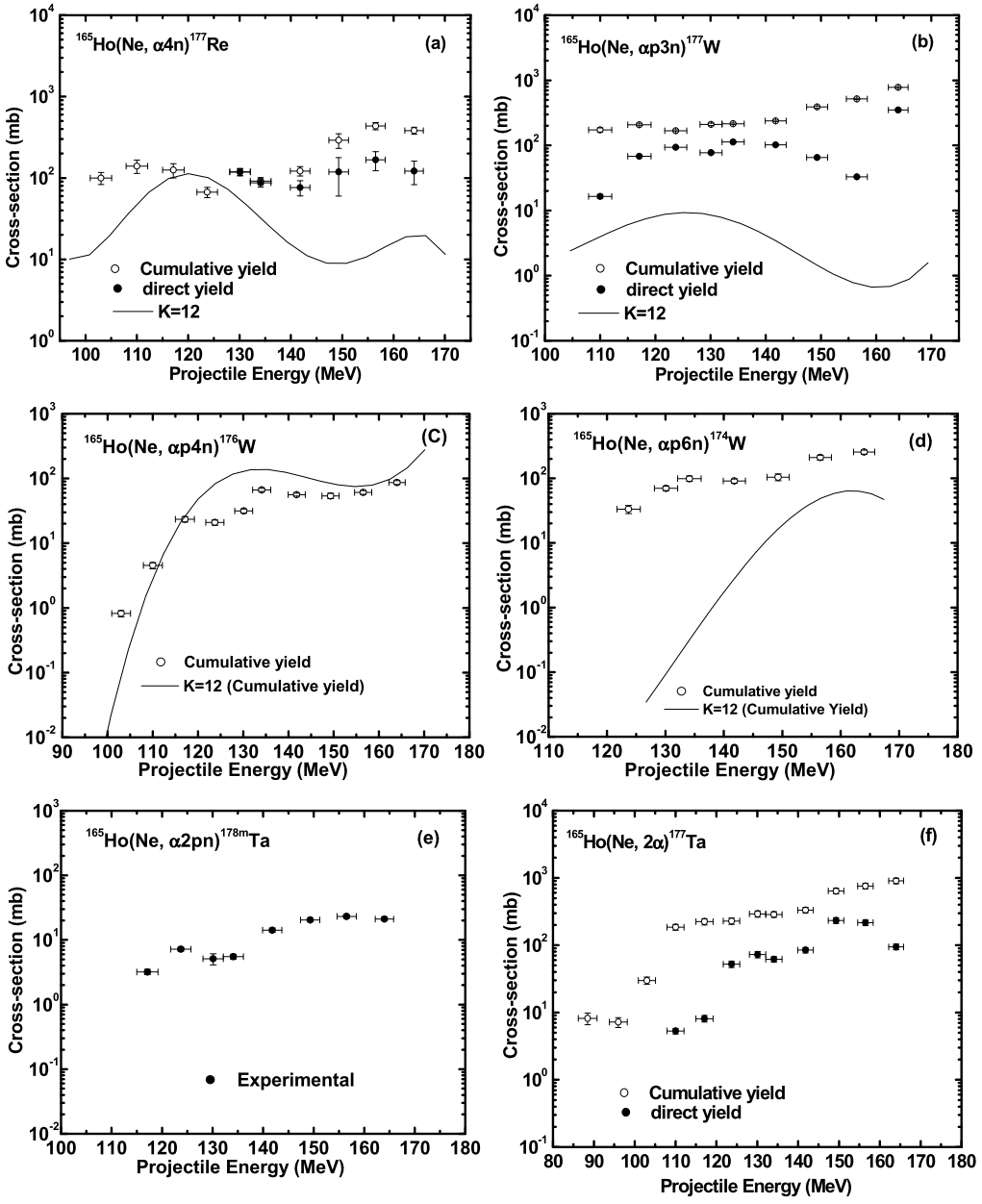

Fig. 3. Excitation functions of the ERs produced in ^{20}Ne + ^{165}Ho reaction. Solid circles represent experimental data. The solid lines correspond to the theoretical predictions of PACE-2 at $K = 12$. Open circles represent the cumulative yield for the production of residue ^{177}Re, ^{177}W, ^{176}W, ^{174}W, ^{178m}Ta, ^{177}Ta and solid circles represent its direct yield.

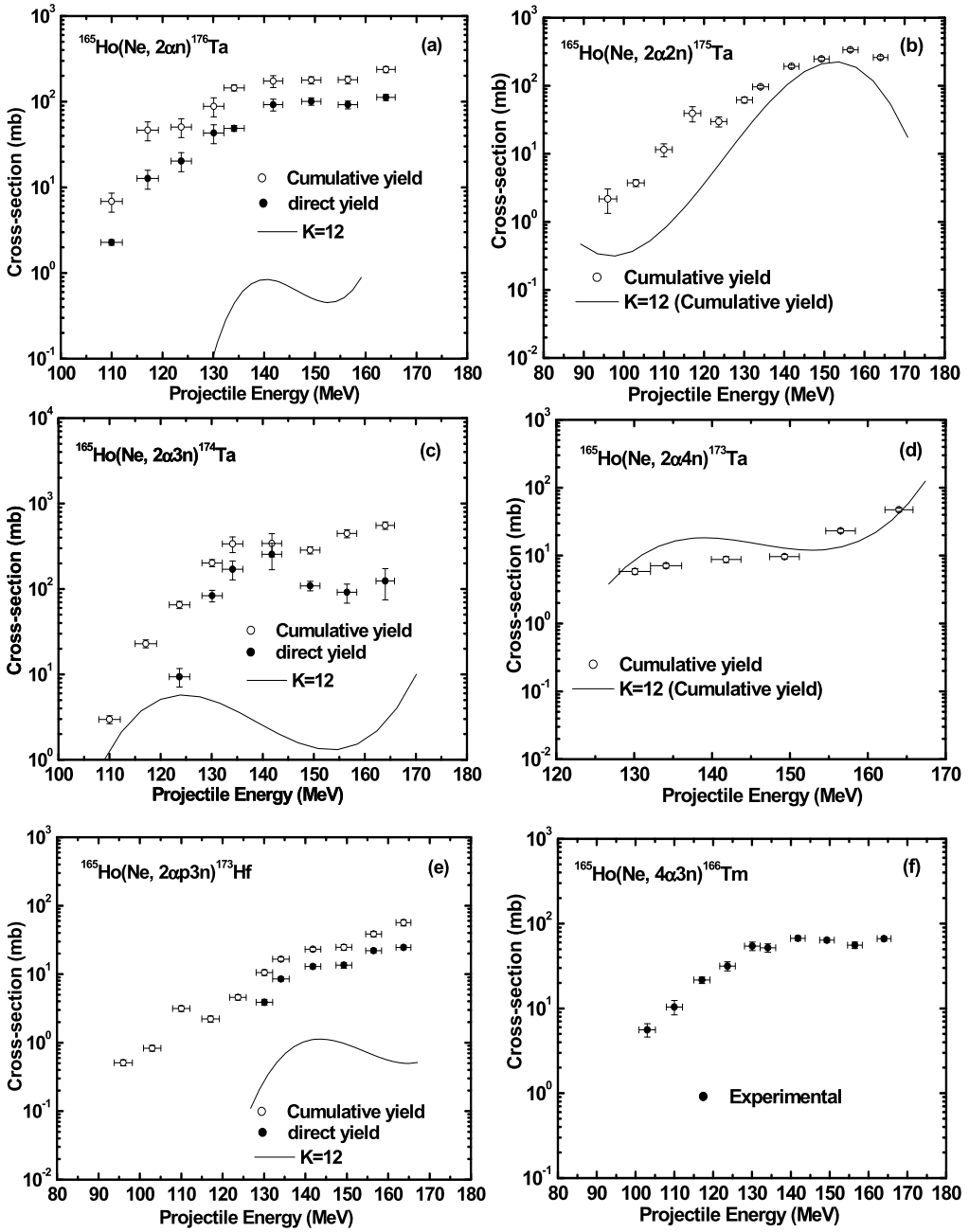

Fig. 4. Excitation functions of the ERs in ^{20}Ne + ^{165}Ho reaction. Solid circles represent experimental data. The solid lines correspond to the theoretical predictions of PACE-2 at $K = 12$. Open circles represent the cumulative yield for the production of residue ^{176}Ta, ^{175}Ta, ^{174}Ta, ^{173}Ta, ^{173}Hf, ^{166}Tm and solid circles represent its direct yield.

time of irradiation. Hence the activity of ^{181}Re measured has significant contribution from the decay of the precursors. This may result in the large errors in the cross-section of ^{181}Re formed by ICF. The excitation energy of incompletely fused composite nucleus ^{181}Re will be sufficiently high to give negligible cross-section of ^{181}Re as evaporation residue from ICF. In Fig. 2(d), the increasing cross-section of ^{181}Re with increasing beam energy could be due to the onset of pre-equilibrium proton emission resulting in high cross-section of ^{181}Os which has not been taken into consideration while calculating the ER cross-sections by PACE-2. Measured cumulative EFs of the residues ^{176}W and ^{174}W produced in αp4n and αp6n emission channels are compared with the PACE-2 cumulative EFs. The experimental values of cross-sections for ^{176}W are found to be comparable with that of theoretical predictions while for residue ^{174}W, much enhancement in the experimental values are observed and shown in Fig. 3(c)–(d). No breakup of projectile is observed for the production of residue ^{176}W, while the production of residue ^{174}W may again be understood in term of ICF in addition to CF of the projectile. The production details of the ERs ^{181}Re is shown by the following reaction equations

The evaporation residue ^{181}Re may be populated via three different reaction modes as follows:

(i) CF of ^{20}Ne with ^{165}Ho i.e.

$$^{20}\mathrm{Ne} + {}^{165}\mathrm{Ho} \rightarrow {}^{185}\mathrm{Ir}^{*} \rightarrow {}^{181}\mathrm{Re} + \alpha$$

(ii) ICF of ^{20}Ne (i.e. fusion of the fragment ^{16}O)

$$^{20}\mathrm{Ne}\ ({}^{16}\mathrm{O} + \alpha) + {}^{165}\mathrm{Ho} \rightarrow {}^{16}\mathrm{O} + {}^{165}\mathrm{Ho} \rightarrow {}^{181}\mathrm{Re}^{*} + \alpha\ (\text{spectator})$$

$$\llcorner\!\!\xrightarrow{\hspace{12em}}\ (\alpha\text{-particle as spectator})$$

(iii) β^{+}/EC-decay of the produced higher charge precursor isobar, i.e.

$$^{20}\mathrm{Ne} + {}^{165}\mathrm{Ho} \rightarrow {}^{181}\mathrm{Os}^{*} + \mathrm{p} + 3\mathrm{n}$$

$$^{181}\mathrm{Os}^{*} \rightarrow {}^{181}\mathrm{Re} + \beta^{+}/\mathrm{EC}$$

Similarly, the residues ^{179}Re, ^{178}Re, ^{177}Re, $^{178\mathrm{m}}$Ta, ^{177}W and ^{174}W may also be populated via three different reaction modes as discussed above. Their EFs are displayed in respective figures.

The ERs ^{177}Ta (2α), ^{176}Ta (2αn), ^{175}Ta (2α2n), ^{174}Ta (2α3n), ^{173}Ta (2α4n) and ^{173}Hf (2αp3n) produced in 2α-emission channels may also be populated by the decay of the produced higher charge precursor isobars. However, from the measured cumulative cross-sections of the ERs ^{177}Ta, ^{176}Ta, ^{174}Ta and ^{173}Hf, the contributions from their respective higher charge precursor isobars ^{177}W, ^{176}W, ^{174}W and ^{173}Ta have been separated out to obtain the contribution of their direct cross-sections. The direct and cumulative cross-sections have been obtained using the expressions given in Table 2 and are displayed in Figs. 3(f), 4(a), 4(c) and 4(e). The enhancement in the measured EFs over their theoretical predictions again indicates the presence of the ICF component along with CF. In Fig. 3(f), the cross-sections for ^{177}Ta by ICF route is expected to be negligible owing to the high excitation energy of ^{177}Ta. Again obtained ICF cross-section of ^{177}Ta would actually be due to the large error in the subtraction of CF cross-section of ^{177}Re and ^{177}W (PACE-2 predictions) from the measured cumulative cross-section of ^{177}Ta. Deduced ICF cross-sections of ^{177}Ta in most of the cases are within 10–15% of the PACE-2 predictions, and hence could be due to erroneous predictions. The measured cumulative cross-section values for the residue ^{175}Ta, as shown in Fig. 4(b), are little higher than the theoretical cumulative cross-section values, indicating the presence of ICF components along with CF. However, the measured cumulative cross-section values for the residue ^{173}Ta, as shown in Fig. 4(d), are found to be comparable with theoretical cumulative cross-section values, thereby showing the negligible effect from the break-up of the projectile ^{20}Ne. The Q_{gg} for the break-up of ^{20}Ne into ^{14}C

and ^{6}Be followed by fusion of ^{14}C with ^{165}Ho is -40 MeV, which is much smaller than that (-25 MeV) for break fusion reaction ^{165}Ho (^{20}Ne, ^{8}Be)^{177}Ta and hence the cross-section for the first reaction can be considered as negligible as compared to the second reaction. The production details of the ERs ^{177}Ta and ^{176}Ta are also shown by the following reaction equations, which are given below.

The residue ^{177}Ta may be populated via two different reaction modes as follows:

(i) ICF of ^{20}Ne (i.e. fusion of fragment ^{12}C)

$$^{20}\mathrm{Ne}[^{12}\mathrm{C} + {}^{8}\mathrm{Be}\ (2\alpha)] + {}^{165}\mathrm{Ho} \rightarrow {}^{12}\mathrm{C} + {}^{165}\mathrm{Ho} \rightarrow {}^{177}\mathrm{Ta}^{*} + 2\alpha\ \text{(spectator)}$$
$$\llcorner\!\!\!\longrightarrow\ [{}^{8}\mathrm{Be}\ (2\alpha)\ \text{as spectator}]$$

(ii) β^{+}/EC-decay of the produced higher charge precursor isobar i.e.

$$^{20}\mathrm{Ne} + {}^{165}\mathrm{Ho} \rightarrow {}^{177}\mathrm{W}^{*} + \alpha + \mathrm{p} + 3\mathrm{n}$$
$$^{177}\mathrm{W}^{*} \rightarrow {}^{177}\mathrm{Ta} + \beta^{+}/\mathrm{EC}$$

As such, the residue ^{176}Ta may be populated via three different reaction modes as follows:

(i) CF of ^{20}Ne with ^{165}Ho, i.e.

$$^{20}\mathrm{Ne} + {}^{165}\mathrm{Ho} \rightarrow {}^{185}\mathrm{Ir}^{*} \rightarrow {}^{176}\mathrm{Ta} + 2\alpha + \mathrm{n}$$

(ii) ICF of ^{20}Ne (i.e. fusion of fragment ^{12}C)

$$^{20}\mathrm{Ne}[^{12}\mathrm{C} + {}^{8}\mathrm{Be}\ (2\alpha)] + {}^{165}\mathrm{Ho} \rightarrow {}^{12}\mathrm{C} + {}^{165}\mathrm{Ho} \rightarrow {}^{177}\mathrm{Ta}^{*} + 2\alpha\ \text{(spectator)}$$
$$\llcorner\!\!\!\longrightarrow\ [{}^{8}\mathrm{Be}\ (2\alpha)\ \text{as spectator}]$$
$$^{177}\mathrm{Ta}^{*} \rightarrow {}^{176}\mathrm{Ta} + \mathrm{n}$$

(iii) β^{+}/EC-decay of the produced higher charge precursor isobar i.e.

$$^{20}\mathrm{Ne} + {}^{165}\mathrm{Ho} \rightarrow {}^{176}\mathrm{W}^{*} + \alpha + \mathrm{p} + 4\mathrm{n}$$
$$^{176}\mathrm{W}^{*} \rightarrow {}^{176}\mathrm{Ta} + \beta^{+}/\mathrm{EC}$$

Similarly, production of the residues ^{175}Ta, ^{174}Ta, ^{173}Ta and ^{173}Hf populated via CF and/or ICF channels may also be understood. The some of the ERs populated in CF or ICF or in both processes in this system. e.g. ^{173}Ta is populated in CF, ^{175}Ta partly in CF and partly in ICF, while remaining Ta isotopes are populated in ICF. The incomplete fusion of ^{12}C with ^{165}Ho following break-up of ^{20}Ne into ^{8}Be + ^{12}C will result in the formation of ^{177}Ta as the incompletely fused composite nucleus, which may dissipate its excitation energy through neutron emission and ultimately leading for ICF products as $^{177-x}$Ta (x = 1, 2, 3, 4). As the excitation of the incompletely fused composite nucleus (^{177}Ta) would be lower than the ^{177}Ta formed during the de-excitation of the compound nucleus (^{185}Ir) through alpha evaporation, ICF will results in formation of higher isotopes of Ta than that in CF. This could be the reason of ^{173}Ta is formed purely in CF, ^{175}Ta partly in CF and partly in ICF, while the higher isotopes are solely formed in ICF. The excitation energy of the incompletely fused composite nucleus (^{177}Ta) formed in incomplete fusion of ^{12}C with ^{165}Ho can be calculated using the formula,

$$E * \left(^{177}\mathrm{Ta}\right) = (12/20) * E\left(^{20}\mathrm{Ne}\right) * (165/177) + Q_{gg}$$

Where $E(^{20}\mathrm{Ne})$ is the laboratory projectile energy and Q_{gg} is the ground state Q value for the break-up fusion reaction. The factor (12/20) is the fraction of the projectile energy with which the projectile like fragment (^{12}C) fused with the target nucleus. The factor (165/177) is the

kinematic factor for lab to center of mass energy. The excitation energy of ^{177}Ta formed ICF varies from 36 to 67 MeV for projectile energy from 110–165 MeV.

In case of evaporation residue ^{166}Tm produced via (4α3n) emissions channel the theoretical prediction of code PACE-2 gives negligible cross-sections (< 0.01 mb), and hence are not shown in Fig. 4(f), while the measured cross-sections are comparatively much larger. This large enhancement in the measured cross-sections over their theoretical predictions may again be attributed to the ICF process of the projectile ^{20}Ne, if ^{20}Ne break-up into ^{4}He and ^{16}O fragments and fusion of ^{4}He fragment with target ^{165}Ho and emission of 3 neutrons takes place from the composite system. Another possibility of ICF process may be understood by the breakup of the projectile ^{20}Ne into ^{8}Be and ^{12}C and fusion of fragment ^{8}Be with the target and emission of 1 α-particle and 3 neutrons from the composite system. The enhanced measured cross-sections for the ERs ^{166}Tm may be attributed to ICF process of the type:

$$^{20}\mathrm{Ne}[^{4}\mathrm{He} + {}^{16}\mathrm{O}\ (4\alpha)] + {}^{165}\mathrm{Ho} \rightarrow {}^{4}\mathrm{He} + {}^{165}\mathrm{Ho} \rightarrow {}^{169}\mathrm{Tm}^{*} + 4\alpha\ \text{(spectator)}$$

$$\llcorner\!\!\longrightarrow [{}^{16}\mathrm{O}\ (4\alpha)\ \text{as spectator}]$$

$$^{169}\mathrm{Tm}^{*} \rightarrow {}^{166}\mathrm{Tm} + 3\mathrm{n}$$

Finally, it may be concluded from the present analysis that the ERs ^{182}Ir (3n), ^{182}Os (p2n), ^{181}Os (p3n), ^{176}W (αp4n) and ^{173}Ta (2α4n) are produced by CF of the projectile while the ERs ^{181}Re (α), ^{179}Re (α2n), ^{178}Re (α3n), ^{177}Re (α4n), ^{177}W (αp3n), ^{174}W (αp6n), $^{178\mathrm{m}}$Ta (α2pn), ^{177}Ta (2α), ^{176}Ta (2αn), ^{175}Ta (2α2n), ^{174}Ta (2α3n), ^{173}Hf (2αp3n) and ^{166}Tm (4α3n) are produced through ICF process, where as the break-up of projectile takes place in the nuclear field. The off line gamma spectrometry technique may not give the cross-sections of all the ERs, as all of them might not have the favorable nuclear decay characteristics, such as, half life, gamma energy and branching intensity. These ERs constitute a small fraction of the total CF. The gamma lined have been assigned for the one ERs ^{175}W (271.4 keV) in Fig. 1. The ERs lower than Ho in Z might also be populated in transfer reactions from target to projectile and through fission. These are $^{154\mathrm{g}}$Tb (123.1 keV), $^{103\mathrm{g}}$Ag (148.6 keV), ^{81}Sr (155.2 keV), $^{129\mathrm{g}}$Ba (223.2 keV), ^{86}Zr (242.9 keV), ^{61}Cu (281.7 keV). The gammas lined have been also assigned for these ERs lower than Ho in Z.

4.3. ICF fraction and observation of mass-asymmetry effect

In the present work, from the experimentally measured EFs, it may not be possible to directly obtain the relative contributions of CF and ICF. However, an attempt has been made to estimate the ICF cross-sections and the dependence of ICF fraction on the projectile energy and entrance channel mass-asymmetry for the present ^{20}Ne + ^{165}Ho system. The production cross-sections which have been measured experimentally may be attributed to the both CF and/or ICF. As already mentioned, the enhancement in the experimentally measured production cross-sections over the PACE-2 predictions in some of the residues may be attributed to ICF process. As such the ICF contribution (σ^{ICF}) for individual channels has been estimated by subtracting theoretically calculated CF cross-section by PACE-2 from the experimentally measured cross-sections at each projectile energy. The total ICF contribution ($\sum \sigma^{\mathrm{ICF}}$) is taken as the sum of cross-sections of all ICF channels at each projectile energy. The ICF cross-section contribution (σ^{ICF})deduced for fifteen ERs are plotted as shown in Fig. 5 along with the sum of all ICF channels cross-section ($\sum \sigma^{\mathrm{ICF}}$) as a function of projectile energy. The solid lines joining the data points are just to guide the eye. In Fig. 5, the resulting excitation functions for ICF do not reveal a systematic dependence

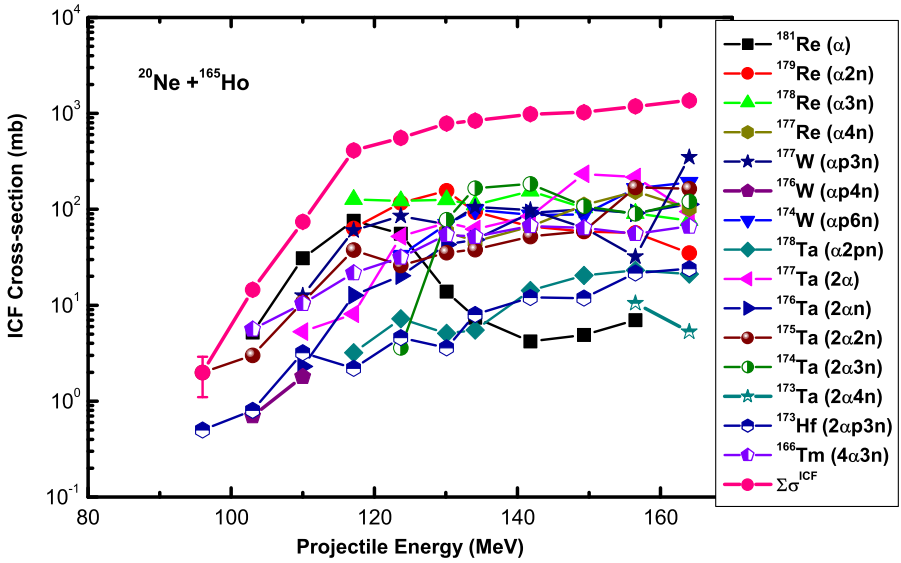

Fig. 5. (Colour online.) Deduced ICF contribution of various ERs produced in ^{20}Ne + ^{165}Ho system as a function of projectile energy. Solid circles represent the sum of all ICF channels ($\sum\sigma^{\mathrm{ICF}}$).

on the number of transferred protons in the ICF process. It is because the ICF processes appear to have a threshold with regard to projectile energy, in that the lowest threshold appears to be for the break-up of the projectile (say ^{20}Ne) into an alpha and ^{16}O, followed by fusion of either of them with the target. This is because as the $\ell_{\max}$ crosses the ℓ_{crit} for CF of projectile and target, break-up of the projectile into alpha and (say ^{16}O) takes place with either of them fusing with the target. At still energy even the ℓ_{crit} for fusion of ^{16}O with target will be crossed and hence another ICF channel opens, wherein ^{20}Ne breaks into ^{8}Be and ^{12}C and either of them could fuse with the target. In this sense the probability of ICF decreases with increasing proton number of the outgoing fragment from the projectile, at a particular energy. In Fig. 5, the cross-section for ^{181}Re is the sum of (^{20}Ne, α) as well as (^{20}Ne, 2p2n) reactions, which has maximum around 120 MeV. The rise in cross-section at higher energies could be due to the onset of pre-equilibrium emission of high energy protons prior to the equilibration of the remaining projectile fragment with the target. Finally, it is quite clear from this figure that the ICF contribution increases with projectile energy and hence reveals that the projectile break-up probability in general increases with projectile energy.

The total CF cross-section ($\sum\sigma^{\mathrm{CF}}$) has been obtained from PACE-2 code, by taking the sum of cross-sections of all CF channels at each projectile energy. Further, the total CF channels cross-section ($\sum\sigma^{\mathrm{CF}}$) and total ICF channels cross-section ($\sum\sigma^{\mathrm{ICF}}$) along with total fusion reaction cross-section ($\sum\sigma^{\mathrm{TF}} = \sum\sigma^{\mathrm{CF}} + \sum\sigma^{\mathrm{ICF}}$) is plotted against projectile energy as shown in Fig. 6(a). From this figure, it has been observed that ICF contributes larger to the production yield with respect to the CF process as the projectile energy is increased, which is quite expected as the break-up probability of the incident ion into α-clusters (i.e. break-up of ^{20}Ne into $^{16}\mathrm{O} + \alpha$ and/or $^{12}\mathrm{C} + {}^{8}\mathrm{Be}$) increases with projectile energy.

In order to estimate the ICF fraction for the present ^{20}Ne + ^{165}Ho system, the ratio of total ICF cross-section ($\sum\sigma^{\mathrm{ICF}}$) to the total fusion cross-section ($\sum\sigma^{\mathrm{TF}}$), defined as ICF fraction, $F^{\mathrm{ICF}} = [\sum\sigma^{\mathrm{ICF}}/(\sum\sigma^{\mathrm{CF}} + \sum\sigma^{\mathrm{ICF}})]$ has been deduced and plotted as a function of projectile

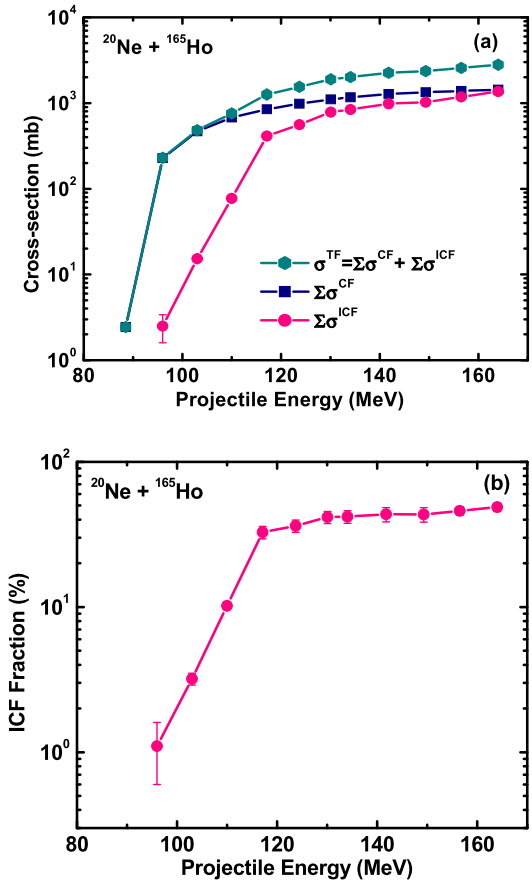

Fig. 6. (Colour online.) (a) Total fusion cross-section ($\sum\sigma^{TF}$) along with the sum of CF cross-sections ($\sum\sigma^{CF}$) and sum of ICF cross-sections ($\sum\sigma^{ICF}$) at different projectile energy for the system ^{20}Ne + ^{165}Ho. (b) ICF-fraction as a function of projectile energy.

energy as shown in Fig. 6(b). It can be seen from this figure that the ICF fraction also increases with projectile energy. This observation shows that the break-up probability of the incident ion into α-clusters (i.e. break-up of ^{20}Ne into ^{16}O + α and/or ^{12}C + ^{8}Be) increases with projectile energy. More over, the ICF-fraction has also been found to increase from $\approx 1\%$ to $\approx 49\%$ at projectile energies between 96–164 MeV.

Morgenstern et al. [26] has suggested that onset of ICF is governed by relative velocity of projectile (V_{rel}), given by:

$$V_{rel} = \sqrt{\frac{2(E_{CM} - E_{CB})}{\mu}} \tag{10}$$

where, μ is the reduced mass of the system, E_{CM} is the centre-of-mass energy and E_{CB} is the Coulomb barrier between two interacting partners. This expression takes into account the difference in Coulomb barrier between each two systems. With this view, the ICF fraction for the present system ^{20}Ne + ^{165}Ho along with previously measured systems ^{20}Ne + ^{55}Mn [24],

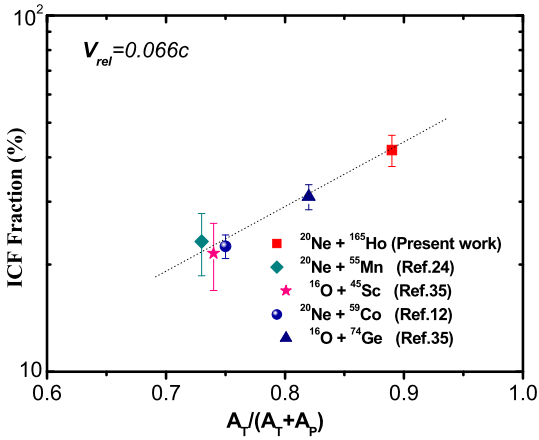

Fig. 7. (Colour online.) Variation of ICF-fraction as a function of entrance channel mass-asymmetry between projectile and target at constant value of $V_{rel} = 0.066c$.

$^{16}O + ^{45}Sc$ [35,36], $^{20}Ne + ^{59}Co$ [12] and $^{16}O + ^{74}Ge$ [35,37] as a function of entrance channel mass-asymmetry $[A_T/(A_T + A_P)]$, for the same relative velocity $V_{rel} = 0.066c$, have been estimated and plotted as a function of mass-asymmetry, between projectile and target as shown in Fig. 7. As can be seen clearly from this figure that the ICF fraction is sensitive to projectile energy and mass-asymmetry of the projectile-target systems and in general ICF probability is more in a mass-asymmetric systems than in mass-symmetric systems.

4.4. Total transfer yields for the measured ICF channels by Sumrule model

Wilczynski et al. [30] explained the ICF reactions in terms of the Sumrule model. The Sumrule model based on the generalized concept of critical angular momentum (ℓ_{crit}), describes that the different ICF channels are populated in the angular momentum (ℓ) space above the ℓ_{crit} for CF. This model predicted the ICF cross-sections at projectile energies above 10.5 MeV/nucleon and the localization of the various reactions in ℓ-space. In the present work we have made an attempt to calculate the cross-sections for CF and ICF channels for ERs formed during the fusion of the fragments of projectile ^{20}Ne with target ^{165}Ho, using the Sumrule model. The model contains three important parameters, namely the temperature of the contact zone between the interacting partners (T), the diffuseness parameter (Δ) of transmission probability distribution (T_ℓ) and the Coulomb interaction radius (R_c). These parameters were taken as 3.5 MeV, 1.7$\hbar$ and 12.3 fm respectively as suggested by Wilczynski et al. [30]. The total transfer yields in ICF reaction channels associated with PLFs in α, 2α and 4α emission channels at projectile energy of 130.1 MeV have been estimated from the measured experimental data and are compared with Sumrule model predictions for the present system and a comparison has been in Table 8.

It has been observed that the measured total transfer yields in ICF reaction channels associated with PLFs in α, 2α and 4α emission channels are obtained as 498.2 mb, 232.7 mb and 54.4 mb respectively and on the other hand Sumrule model predicted values are 121.2 mb, 32.3 mb and 9.7 mb respectively, which are much smaller than the experimental total transfer yields. Finally, it can also be observed from Table 8 (last row) that Sumrule calculations account for only 21% of the experimental ICF cross-section at this projectile energy. This shows that Sumrule model

Table 8
Experimentally measured and theoretically (Sumrule model) calculated total transfer yields in ICF reaction channels associated with PLFs in α, 2α and 4α-emission channels.

Measured evaporation residues	σ_{Exp} (mb)	σ_{PACE} (mb)	Experimental σ_{ICF} (mb) = σ_{Exp} (mb) − σ_{PACE} (mb)	Transfer yield $\sigma_{Sumrule}$ (mb)
PLFs (1α-emission channels)				
^{181}Re (α)	13.9	–	13.9	
^{179}Re (α2n)	162.7	7.5	155.2	
^{178}Re (α3n)	130.0	3.9	126.1	
^{177}Re (α4n)	118.4	59.6	58.8	
^{177}W (αp3n)	77.5	8.3	69.2	
^{174}W (αp6n)	70.0*	0.11*	69.9	
^{178}Ta (α2pn)	5.5	–	5.5	
Total 1α-emission transfer yield			498.2	121.2
PLFs (2α-emission channels)				
^{177}Ta (2α)	72.8	–	72.8	
^{176}Ta (2αn)	43.1	0.11	43.0	
^{175}Ta (2α2n)	61.8*	26.3*	35.5	
^{174}Ta (2α3n)	83.4	5.6	77.8	
^{173}Hf (2αp3n)	3.9	0.3	3.6	
Total 2α-emission transfer yield			232.7	32.3
PLFs (4α-emission channels)				
^{166}Tm (4α3n)	54.4	–	54.4	
Total 4α-emission transfer yield			54.4	9.7
Total transfer yield			785.3	163.2

* Cumulative cross-sections.

does not work below 8 MeV/A, as observed earlier by Babu et al. [48], Singh et al. [25] and Ali et al. [24].

4.5. Critical angular momentum (ℓ_{crit}) calculation using Bass model

An attempt has been made to calculate the critical angular momentum (ℓ_{crit}) from the experimentally measured total ER cross-sections at different projectile energies and are compared with Bass model predictions (using PACE-2). A comparison has been shown in Table 9. It is found that the ℓ_{crit} values calculated from the experimentally measured total ER cross-sections at lower projectile energies are slightly lower than the Bass model predictions. The low values of ℓ_{crit} associated with ICF-channels suggests that at lower projectile energies, ICF may not be strictly associated with peripheral collision. Instead there appears to be deeper penetration of the projectile with the target at lower beam energy. But at higher projectile energies, the ℓ_{crit} values evaluated from experimentally measured total ER cross-sections are consistent with values obtained from Bass model predictions. This shows that ℓ_{crit}-values associated with ICF channels at higher projectile energy may be associated with ℓ-values lower than that of peripheral collisions, indicating that incomplete fusion competes with complete fusion even at angular momentum values lower than critical angular momentum.

Table 9
Comparison of experimentally measured and theoretically calculated critical angular momentum (ℓ_{crit}).

Projectile energy (MeV)	Critical angular momentum (ℓ_{crit})	
	Experimentally measured (using total ER cross-sections)	Bass formula (using PACE-2)
88.5	–	1
96.0	6	22
103.0	17	33
110.0	25	42
117.1	41	48
123.1	44	53
130.1	53	58
134.1	57	60
141.8	64	65
149.3	68	68
156.5	74	71
163.7	80	74

5. Summary and conclusions

The EFs for eighteen ERs produced in CF and/or ICF process have been measured in ^{20}Ne + ^{165}Ho systems in the projectile energy range $\approx$ 4–8 MeV/A. Many of the ERs are populated both directly and in the decay of the precursor isobars. An attempt has been made to deduce the direct production cross-sections from the measured cumulative cross-sections and precursor decay contributions of different radio-nuclides. The experimentally measured EFs have been compared with PACE-2 predictions, after correcting for the precursor contributions. It has been observed that EFs for the ERs produced through CF channels ^{182}Ir (3n), ^{182}Os (p2n) and ^{181}Os (p3n) are well reproduced with PACE-2 predictions, while the ERs produced in ICF channels ^{181}Re (α), ^{179}Re (α2n), ^{178}Re (α3n), ^{177}Re (α4n), ^{177}W (αp3n), ^{174}W (αp6n), ^{178m}Ta (α2pn), ^{177}Ta (2α), ^{176}Ta (2αn), ^{175}Ta (2α2n), ^{174}Ta (2α3n), ^{173}Hf (2αp3n) and ^{166}Tm (4α3n) show significant enhancement over PACE-2 predictions. This enhancement may be attributed to the fact that these ERs have been populated not only by CF of ^{20}Ne with ^{165}Ho but also populated through ICF process where as the projectile break-up into α-clusters (i.e. ^{20}Ne break-up into fragments ^{16}O + α and/or ^{12}C + ^{8}Be) and fusion of one of the clusters may take place with target nucleus. The experimental values of cross-sections for ERs ^{176}W (αp4n) and ^{173}Ta (2α4n) are found to be comparable with that of theoretical predictions. No breakup of projectile is observed for the production of ERs ^{176}W (αp4n) and ^{173}Ta (2α4n). The analysis of the data also suggests that ICF probability increases with projectile energy. Hence, it has been found that the ICF fraction of the total fusion cross-section also increases with projectile energy. The analysis of the present data also suggests that the projectile break-up probability leading to ICF increases with projectile energy. The present observation thus supports the Morgenstern systematics [26]. The comparison of the present data with similar data on ^{20}Ne + ^{55}Mn [24], ^{16}O + ^{45}Sc [35,36], ^{20}Ne + ^{59}Co [12] and ^{16}O + ^{74}Ge [35,37] systems suggest that ICF probability increases in mass-asymmetric system than in mass-symmetric system, supports the previous findings [12,24,26–28]. The comparison of the experimental total transfer yields with theoretical total transfer yields deduced by Sumrule model suggests that the Sumrule model in its present form is unable to predict the cross-sections of the ERs produced in ICF channel at projectile energy $\approx$ 6 MeV/A. From the present experimental data, it has been also observed that the ℓ_{crit} values associated with ICF channels at higher projectile energy may be associated with peripheral collisions. These observations sug-

gest that ICF competes with CF even at ℓ values lower than ℓ_{crit}. It is also worth to mention that at projectile energy below 8 MeV/A, ICF process plays an important role for the estimation of total reaction cross-section. Further, a large number of experimental data is needed for various projectile-target combinations. Measurement of spin distributions and feeding intensity pattern of the ERs populated by CF and ICF using particle-gamma coincidence technique at the above projectile energies may provide a better understanding of ICF process.

Acknowledgements

The authors are grateful to the Director, VECC, Kolkata, for providing the experimental facilities to carry out the experiment. The authors are also thankful to Dr. S.K. Basu, Dr. S.K. Saha and operational staff of Cyclotron, VECC, Kolkata for providing the necessary facilities and good co-operation during the course of this experiment. The authors are very much thankful to Dr. R. Tripathi, Radio-chemistry Division, Bhabha Atomic Research Centre, Mumbai, for valuable discussion and time-to-time help and co-operation through out this work. The authors are also thankful to the Chairman, Department of Physics, A.M.U., Aligarh, India, for providing the necessary facilities related with this research work. Financial support provided by UGC-DAE-CSR, Kolkata and University Grants Commission, New Delhi are also acknowledged gratefully. One of the author D. Singh is also thankful to the Council of Scientific and Industrial Research (CSIR), New Delhi for providing the financial support during this research work.

References

[1] Ch. Ngo, Prog. Nucl. Part. Phys. 16 (1985) 139.
[2] P.E. Hodgson, Nuclear Heavy Ion Reactions, Clarendon Press, Oxford, 1978.
[3] P.E. Hodgson, E. Gadioli, E. Gadioli Erba, Introductory Nuclear Physics, Clarendon Press, Oxford, 1997.
[4] M. Cavinato, et al., in: Heavy Ion Fusion, A.M. Stefanini (Ed.), Singapore, World Scientific, 1994.
[5] G.D. Dracoulis, A.P. Byrne, T. Kibedi, T.R. Mcgoram, S.M. Mullins, J. Phys. G: Nucl. Part. Phys. 23 (1997) 1191.
[6] D.J. Parker, J.J. Hogan, J. Asher, Phys. Rev. C 39 (1989) 2256.
[7] M. Crippa, E. Gadioli, G. Ciavola, C. Marchetta, M. Bonardi, Z. Phys. A 350 (1994) 121.
[8] B.S. Tomar, A. Goswami, A.V.R. Reddy, S.K. Das, P.P. Burte, S.B. Manohar, Phys. Rev. C 49 (1994) 941.
[9] B. Bindu Kumar, S. Mukherjee, S. Chakrabarty, B.S. Tomar, A. Goswami, S.B. Manohar, Phys. Rev. C 57 (1998) 743.
[10] M.K. Sharma, B.P. Singh, Unnati, R. Kumar, K.S. Golda, H.D. Bhardwaj, R. Prasad, Nucl. Phys. A 776 (2006) 83; M.K. Sharma, B.P. Singh, Unnati, R. Kumar, K.S. Golda, H.D. Bhardwaj, R. Prasad, Phys. Rev. C 70 (2004) 044606.
[11] D. Singh, R. Ali, M. Afzal Ansari, M.H. Rashid, R. Guin, S.K. Das, Phys. Rev. C 79 (2009) 054601.
[12] D. Singh, R. Ali, M. Afzal Ansari, B.S. Tomar, M.H. Rashid, R. Guin, S.K. Das, Phys. Rev. C 83 (2011) 054604.
[13] H.C. Britt, A.R. Quinton, Phys. Rev. 124 (1964) 877.
[14] J. Galin, B. Gatty, D. Guirean, C. Rousset, V.C. Schlot-thauervoos, X. Tarrago, Phys. Rev. C 9 (1974) 1126.
[15] T. Inamura, M. Ishihara, T. Fakuda, T. Shimoda, H. Hiruta, Phys. Lett. B 68 (1977) 51.
[16] D.J. Parker, J. Asher, T.W. Colon, N. Naquib, Phys. Rev. C 30 (1984) 143.
[17] I. Tserruya, V. Steiner, Z. Fraenkel, P. Jacobs, D.G. Kovar, W. Henning, M.F. Vineyard, B.G. Glagela, Phys. Rev. Lett. 60 (1988) 14.
[18] P.R.S. Gomes, I. Padron, M.D. Rodriguez, G.V. Marti, R.M. Anjos, J. Lubian, R. Veiga, R. Liguori Neto, E. Crema, N. Added, L.C. Chamon, J.O. Fernandez Niello, O.A. Capurro, A.J. Pacheco, J.E. Testoni, D. Arbiola, A. Arazi, M. Ramirez, M.S. Hussein, Phys. Lett. B 601 (2004) 20.
[19] P. Vergani, E. Gadioli, E. Vaciago, E. Fabrici, E. Gadioli Erba, M. Galmarini, G. Ciavola, C. Marchetta, Phys. Rev. C 48 (1993) 1815.
[20] M. Cavinato, E. Fabrici, E. Gadioli, E. Gadioli Erba, P. Vergani, M. Crippa, G. Colombo, I. Redaelli, M. Ripamonti, Phys. Rev. C 52 (1995) 2577.
[21] M. Crippa, E. Gadioli, G. Ciavola, C. Marchetta, M. Bonardi, Z. Phys. A 350 (1994) 121.

[22] B.S. Tomar, A. Goswami, G.K. Gubbi, A.V.R. Reddy, S.B. Manohar, John Bency, S.K. Katraria, Phys. Rev. C 58 (1998) 3478.
[23] U. Gupta, P.P. Singh, D.P. Singh, M.K. Sharma, A. Yadav, R. Kumar, B.P. Singh, R. Prasad, Nucl. Phys. A 811 (2008) 77.
[24] R. Ali, D. Singh, M. Afzal Ansari, M.H. Rashid, R. Guin, S.K. Das, J. Phys. G: Nucl. Part. Phys. 37 (2010) 115101.
[25] P.P. Singh, M.K. Sharma, D.P. Singh, Unnati, R. Kumar, K.S. Golda, B.P. Singh, R. Prasad, Eur. Phys. J. A 34 (2007) 29;
P.P. Singh, M.K. Sharma, D.P. Singh, Unnati, R. Kumar, K.S. Golda, B.P. Singh, R. Prasad, Phys. Rev. C 77 (2008) 014607.
[26] H. Morgenstern, W. Bohne, W. Galster, K. Grabisch, A. Kyanowski, Phys. Rev. Lett. 52 (1984) 1104.
[27] M.F. Vineyard, J.S. Bauer, J.F. Crum, C.H. Gosdin, R.S. Trotter, D.G. Kovar, C. Beck, D.J. Henderson, R.V.F. Janssens, B.D. Wilkins, C.F. Maguire, J.F. Mateja, F.W. Prosser, G.S.F. Stephens, Phys. Rev. C 45 (1992) 1784.
[28] S. Chakrabarty, B.S. Tomar, A. Goswami, G.K. Gubbi, S.B. Manohar, A. Sharma, B.B. Kumar, S. Mukherjee, Nucl. Phys. A 678 (2000) 355.
[29] T. Udagawa, T. Tamura, Phys. Rev. Lett. 45 (1980) 1311.
[30] J. Wilczynski, K. Siwek-Wilezynaski, J. Van-Driel, S. Gonggrijp, D.C.J.M. Hageman, R.V.F. Janssens, J. Lukasiak, R.H. Siemssen, S.Y. Van der Werf, Nucl. Phys. A 373 (1982) 109.
[31] J.P. Bondrof, J.N. De, G. Fai, A.O.T. Karvinen, J. Randrup, Nucl. Phys. A 333 (1980) 285.
[32] M.I. Sobel, P.J. Siemens, J.P. Bondrof, H.A. Bethe, Nucl. Phys. A 251 (1975) 502.
[33] V. Zegrebaev, Y. Penionzhkevich, Prog. Part. Nucl. Phys. 35 (1995) 575.
[34] A. Gavron, Phys. Rev. C 21 (1980) 230.
[35] D. Singh, PhD Thesis, Aligarh Muslim University, Aligarh, India, 2008.
[36] D. Singh, M. Afzal Ansari, R. Ali, N.P.M. Sathik, M. Ismail, J. Phys. Soc. Japan 75 (2006) 104201.
[37] D. Singh, M. Afzal Ansari, R. Ali, N.P.M. Sathik, M. Ismail, Chin. J. Phys. 46 (2008) 27.
[38] D. Singh, R. Ali, M. Afzal Ansari, K. Surendra Babu, P.P. Singh, M.K. Sharma, B.P. Singh, R.K. Sinha, Rakesh Kumar, S. Muralithar, R.P. Singh, R.K. Bhowmik, Phys. Rev. C 81 (2010) 027602.
[39] J.F. Ziegler, SRIM-2006, The Stopping Power and Range of Ions in Matter, 2006.
[40] B. Wilken, T.A. Fritz, Nucl. Instr. Meth. 138 (1976) 331.
[41] MAESTRO, Data acquisition and analysis software coupled with EG & G ORTEC hardware.
[42] FREEDOM, Data acquisition and analysis system designed to support the accelerator based experiments at the Inter University Accelerator Centre, New Delhi, India.
[43] M. Afzal Ansari, R.K.Y. Singh, M.L. Sehgel, V.K. Mittal, D.K. Avasthi, I.M. Govil, Ann. Nucl. Energy 11 (1984) 173.
[44] R.B. Firestone, V.S. Shirley, Table of Isotopes, 8th edition, Wiley, New York, 1996.
[45] R. Bass, Nucl. Phys. A 231 (1974) 45.
[46] P.M. Endt, At. Data. Nucl. Data Tables 26 (1981) 47.
[47] A.H. Wapstra, G. Audi, Nucl. Phys. A 4 (1985) 32.
[48] K.S. Babu, R. Tripathi, K. Sudarshan, B.D. Srivastava, A. Goswami, B.S. Tomar, J. Phys. G: Nucl. Part. Phys. 29 (2003) 1011.